Visualizing the spatial organization of monocytes, interstitial macrophages, and tissue-specific macrophages in situ

Maxime Petit, Eléonore Weber-Delacroix, François Lanthiez, Sandrine Barthélémy, Noëlline Guillou, Marina Firpion, Olivia Bonduelle, David A Hume, Christophe Combadière, Alexandre Boissonnas

▶ **To cite this version:**

Maxime Petit, Eléonore Weber-Delacroix, François Lanthiez, Sandrine Barthélémy, Noëlline Guillou, et al.. Visualizing the spatial organization of monocytes, interstitial macrophages, and tissue-specific macrophages in situ. Cell Reports, 2024, 43 (10), pp.114847. 10.1016/j.celrep.2024.114847 . hal-04889092

HAL Id: hal-04889092

https://hal.sorbonne-universite.fr/hal-04889092v1

Submitted on 15 Jan 2025

HAL is a multi-disciplinary open access archive for the deposit and dissemination of scientific research documents, whether they are published or not. The documents may come from teaching and research institutions in France or abroad, or from public or private research centers.

L'archive ouverte pluridisciplinaire **HAL**, est destinée au dépôt et à la diffusion de documents scientifiques de niveau recherche, publiés ou non, émanant des établissements d'enseignement et de recherche français ou étrangers, des laboratoires publics ou privés.

Distributed under a Creative Commons Attribution 4.0 International License

Cell Reports

Article

Visualizing the spatial organization of monocytes, interstitial macrophages, and tissue-specific macrophages *in situ*

Graphical abstract

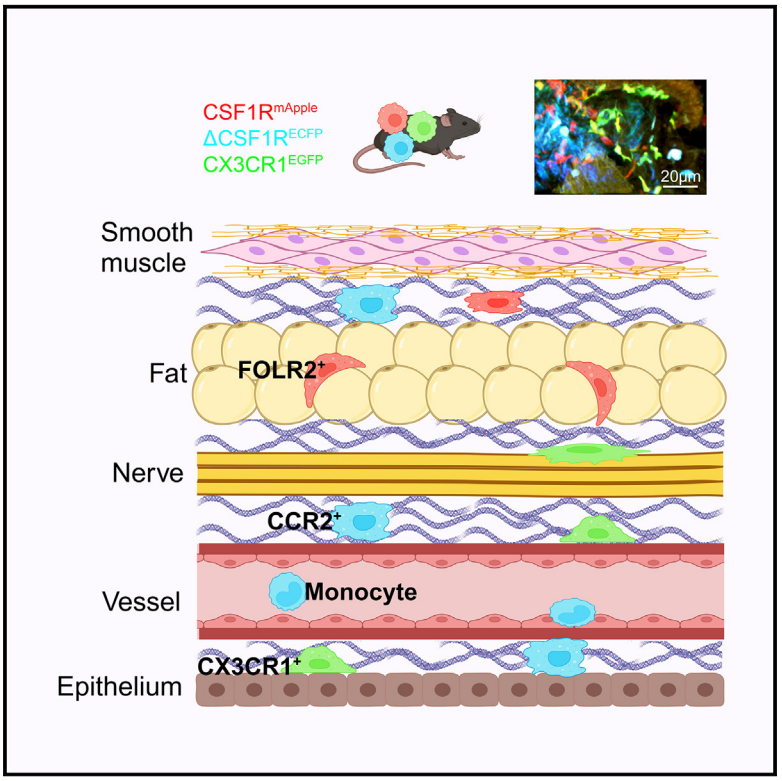

Authors

Maxime Petit, Eléonore Weber-Delacroix, François Lanthiez, ..., David A. Hume, Christophe Combadière, Alexandre Boissonnas

Correspondence

alexandre.boissonnas@upmc.fr

In brief

Petit et al. show that the different mononuclear phagocyte subsets in non-lymphoid organs are spatially organized according to distinct sub-territories and depend on different molecular regulators. This spatial mapping provides a better understanding of the diversity of the mononuclear phagocyte system across different tissues.

Highlights

- Tissue-resident macrophage subsets are associated with distinct sub-anatomic territories
- Tissue-resident macrophage subsets harbor distinct molecular dependencies
- The RGB-Mac mouse discriminates three common interstitial macrophage subsets across tissues

Petit et al., 2024, Cell Reports *43*, 114847
October 22, 2024 © 2024 The Author(s). Published by Elsevier Inc.
https://doi.org/10.1016/j.celrep.2024.114847

CellPress

Cell Reports

CellPress
OPEN ACCESS

Article

Visualizing the spatial organization of monocytes, interstitial macrophages, and tissue-specific macrophages *in situ*

Maxime Petit,[1,3] Eléonore Weber-Delacroix,[1,3] François Lanthiez,[1] Sandrine Barthélémy,[1] Noëlline Guillou,[1] Marina Firpion,[1] Olivia Bonduelle,[1] David A. Hume,[2] Christophe Combadière,[1] and Alexandre Boissonnas[1,4,*]

[1]Sorbonne Université , Inserm U1135, CNRS ERL 8255, Centre d'Immunologie et des Maladies Infectieuses (CIMI-Paris), Paris, France
[2]Mater Research Institute-University of Queensland, Translational Research Institute, Brisbane, QLD, Australia
[3]These authors contributed equally
[4]Lead contact
*Correspondence: alexandre.boissonnas@upmc.fr
https://doi.org/10.1016/j.celrep.2024.114847

SUMMARY

Tissue-resident mononuclear phagocytes (MPs) are an abundant cell population whose localization *in situ* reflects their identity. To enable assessment of their heterogeneity, we developed the red/green/blue (RGB)-Mac mouse based upon combinations of *Cx3cr1* and *Csf1r* reporter transgenes, providing a complete visualization of their spatial organization *in situ*. 3D-multi-photon imaging for spatial mapping and spectral cytometry employing the three markers in combination distinguished tissue-associated monocytes, tissue-specific macrophages, and three subsets of connective-tissue-associated MPs, including CCR2^{+} monocyte-derived cell, CX3CR1^{+}, and FOLR2^{+} interstitial subsets, associated with distinct sub-anatomic territories. These populations were selectively reduced by blockade of CSF1, CSF2, CCR2, and CX3CR1 and efficiently reconstitute their spatial distribution after transient myelo-ablation, suggesting an autonomous regulatory environment. Our findings emphasize the organization of the MP compartment at the sub-anatomic level under steady-state conditions, thereby providing a holistic understanding of their relative heterogeneity across different tissues.

INTRODUCTION

Tissue-resident mononuclear phagocytes (MPs), including monocytes, macrophages, and dendritic cells (DCs), are part of the MP system (MPS), serving as innate immune sentinels, initiating and mediating acquired immunity and contributing to development, homeostasis, and tissue repair. MPS cells adapt to perform specific functions in each tissue[1–4] associated with tissue-specific gene expression and defined cell surface receptors commonly employed as markers.[5] Alongside tissue-specific macrophages, all tissues contain interstitial macrophages located within sub-anatomic structures. Increasingly, single-cell RNA sequencing analysis has defined these subpopulations associated with the vasculature, connective tissue, and nervous tissue,[6–8] although there are significant caveats to interpretation of such data.[9] Cross-tissue comparison in humans and mice defined MPS cell subsets present in multiple organs.[6,10] They include macrophages expressing *Timd4*, *Lyve1, Folr2* transcripts (TLF^{+}), major histocompatibility complex (MHC)-II^{high} macrophages and CCR2^{+} monocyte-derived macrophages.[6] Further heterogeneity was characterized based on the expression of *Mrc1* (CD206) and conserved chemokine signatures across tissue.[11] Classical DCs, especially the cDC2 subset, are difficult to define as a separate entity in non-lymphoid tissues but may constitute a fourth subset.[5] Tissue-specific functional adaptation is guided by interactions with the extracellular matrix and neighboring cells as well as the composition of surrounding factors collectively defined as the macrophage "niche."[12]

The use of fluorescent reporter mice to track MPs *in situ*, through imaging and flow cytometry, has significantly enhanced our understanding of their tissue localization, dynamics, and functions.[13] We previously introduced the RGB-Mac mouse, a triple-fluorescent reporter mouse generated by intercrossing three commonly used transgenic fluorescent mouse strains.[13,14] The *Csf1r*-mApple transgene[15] shows the same ubiquitous expression in myeloid cells, including tissue macrophages and DCs, as observed in the *Csf1r*-EGFP transgenic reporter line.[16] The knockin *Cx3cr1*$^{egfp/+}$ reporter[17] and the MacBlue binary transgene (Csf1r-gal4/vp16/UAS-enhanced cyan fluorescent protein [ECFP]),[18] in which the *Csf1r* promoter region contains a 105-bp deletion that removes an element required for expression of the ECFP reporter in most mature mouse tissue macrophages,[19] resulted in a lack of ECFP expression from nearly all tissue macrophages except alveolar macrophages, some peritoneal macrophages, and most microglial cells in the brain.[20] Here we utilize the RGB-Mac mouse to locate tissue monocytes and distinct populations of resident macrophages within distinct sub-anatomic territories within the liver, lung, kidney, visceral

This is an open access article under the CC BY license (http://creativecommons.org/licenses/by/4.0/).

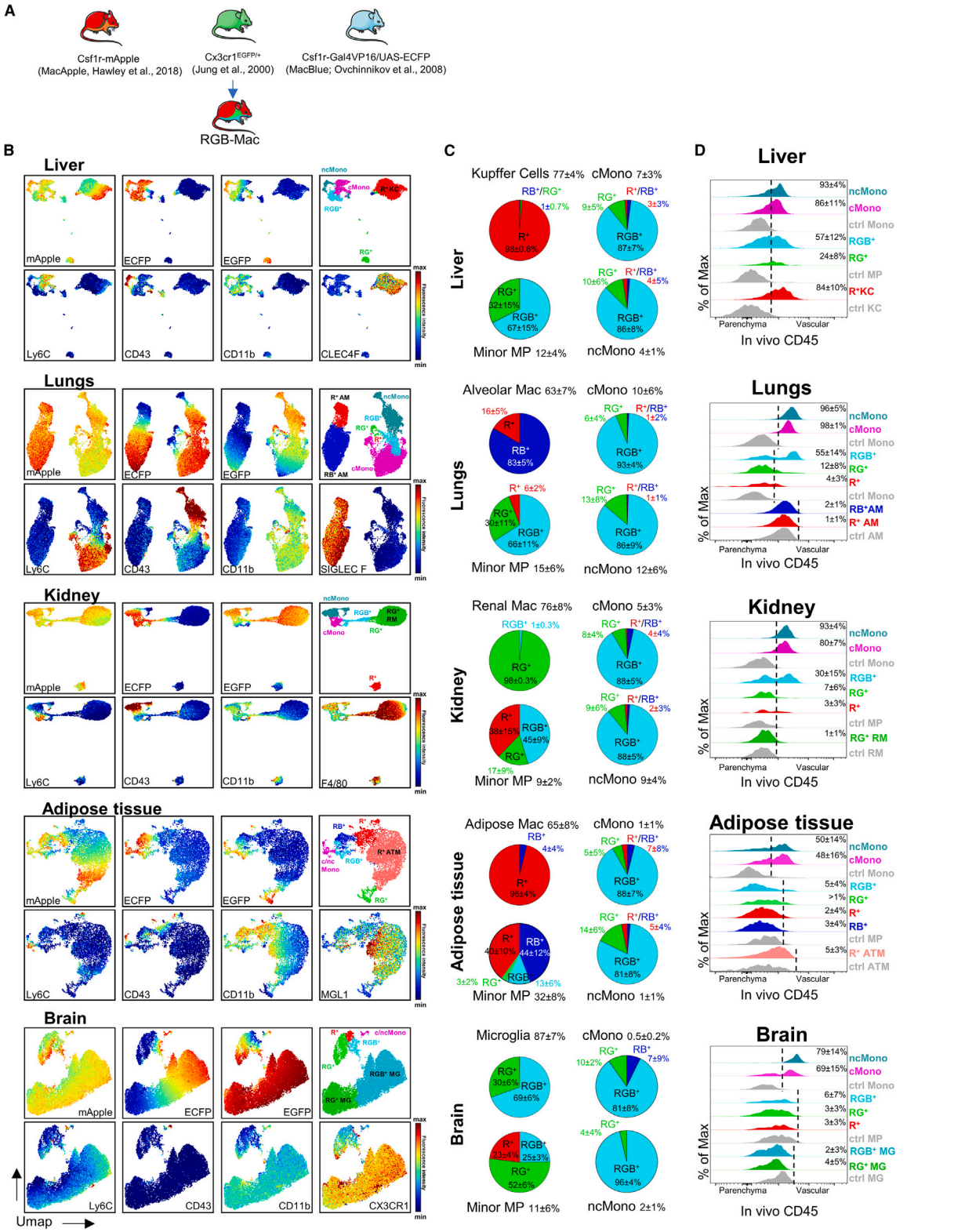

Figure 1. Tissue-resident macrophages and monocytes harbor distinct fluorescent patterns in RGB-Mac mouse

(A) The RGB-Mac mouse model results of the intercross between the Csf1r-mApple transgenic mouse (red), the *Cx3cr1*$^{egfp/+}$ knockin (green), and the Csf1r-Gal4VP16/UAS-ECFP transgenic mouse (blue).

(legend continued on next page)

adipose tissue (AT), and brain. We demonstrate that monocyte and macrophage subsets were able to recover their spatial distribution after systemic myelo-ablation and were selectively depleted by inhibition of CSF1, CSF2, CCR2, and CX3CR1. The results indicate that subsets in defined locations are regulated autonomously in steady-state homeostasis.

RESULTS

Tissue-resident macrophages and monocytes harbor distinct fluorescent patterns in RGB-Mac mouse

We first performed flow cytometry on cells isolated from five non-lymphoid tissues (liver, lung, kidney, visceral adipose, and brain) to define subpopulations of cells expressing different combinations of the reporters (mApple, EGFP, and ECFP) (Figure 1A). The macrophage colony-stimulating factor receptor (CSF1R, also known as CD115) is expressed exclusively in MPS cells.[21] Granulocytes express *Csf1r* mRNA but do not express the CSF1R protein[22]; hence, they express the fluorescent reporters ECFP and mApple but at lower level compared to MP.[15] Among mApple$^{low/-}$ cells, only a subset of natural killer (NK) and T cells are known to express the EGFP but not ECFP, and DC express both with an intermediate level of mApple.[13] We followed the gating strategy (Figure S1A) to define classical monocytes (cMono, defined by Ly6C$^+$ expression, pink gate), non-classical monocytes (ncMono, defined by CD43$^+$ expression, teal gate),[23] and tissue-resident macrophages (CD64$^+$F4/80$^+$, brick red gate). Among these, F4/80^{high}CD11b^{low} macrophages formed the majority cell population isolated from the liver, lung, kidney, and visceral AT. CD11b$^+$F4/80$^+$ macrophages, cMono, and ncMono were less abundant (Figure S1B). In the brain, F4/80^{high}CD11b^{high} were the predominant population, known as microglia (Figure S1B). Relative expression of ECFP and EGFP among all these populations indicated further heterogeneity across tissues (Figure S1A). Four fluorescent signatures were defined: (1) cells expressing only mApple (red [R$^+$], red gate); (2) cells expressing mApple and high level of EGFP (red/green [RG$^+$], green gate); (3) cells expressing mApple and high level of ECFP (red/blue [RB$^+$], blue gate); and (4) cells expressing mApple, high level of ECFP, and various levels of EGFP (red/green/blue [RGB$^+$], cyan gate) (Figure S1A lower panels).

To better characterize the different fluorescent MP subsets across tissues, we generated Uniform Manifold Approximation and Projection (UMAP) among mApple$^+$ CD64$^{low/+}$ and F4/80$^{low/+}$ cells (according to the gating strategy; Figure S1A) and additional well-established phenotypic markers of tissue-specific macrophages (CLEC4F for liver tissue-resident macrophages [TRMs],[24] SIGLEC-F for lung TRMs,[10] F4/80 for renal TRMs,[24] MGL1 for AT TRMs,[25] and CX3CR1 for brain microglia[26]), as well as functional markers (MHC-II, CD206, CD163, TIM4) (Figures 1B and S2). For each tissue, we defined clusters corresponding to classical (pink), non-classical monocytes (teal), the tissue-specific resident macrophages, and the various minor MPs according to their fluorescent signature: RGB$^+$ (cyan), RG$^+$ (green), RB$^+$ (blue) and R$^+$ (red) (Figures 1B and S2).

In parallel, we assessed the expression of the fluorescent reporters on the DC compartment.[27] We gated on F4/80$^-$ CD64$^-$ CD11c$^+$MHC-II$^+$ for CD11b$^+$DCs and on CD11c$^+$MHC-II$^+$ CD103$^+$ for CD103$^+$DCs (Figure S3A). CD103$^+$DCs exhibited lower expression of mApple compared to TRMs in every tissue, and there was no expression of EGFP. In contrast, CD11b$^+$DC expressed lower expression of mApple compared to tissue macrophages but similar expression of ECFP and various levels of EGFP (Figure S3B). As noted by others,[5,28] the distinction between CD64$^{low/+}$ F4/80$^{low/+}$ CD11b$^+$ cDC2 and MHC-II$^+$ tissue macrophages is equivocal. For the purpose of the current study, they are considered as a single entity referred to as MPs.

We quantified the relative proportion of these subsets in every tissue (Figure 1C). The majority of tissue-associated monocytes and circulating monocytes expressed the three fluorescent proteins (RGB$^+$), although EGFP expression level on cMonos was lower compared to other ncMonos, as expected.[17] A subset of both monocyte populations lacked detectable ECFP (RG$^+$) (Figures 1C and S1A) but this was not associated with any other monocyte markers (Figures 1B and S2). The monocyte signatures were conserved across the different organs (Figure 1C) and blood monocytes (Figure S1C). In contrast, the fluorescent signatures among macrophages were more tissue specific (Figure 1C).

In the liver, the dominant population was CD11b^{low}, CLEC4F$^+$, and TIM4$^+$ corresponding to the phenotype of Kupffer cells (KCs).[29] KCs expressed mApple (R$^+$ KCs). Only 0.6% were RGB$^+$ and 0.7% RG$^+$ (Figures 1B, 1C, and S2 liver panels). By contrast, the minor resident MP populations, representing 12% ± 4% of the total, as reported by others,[30] were either RG$^+$ or RGB$^+$ (Figure 1C, liver panels).

In the lungs, the dominant MP population corresponded to alveolar macrophages (AMs) defined as CD11b^{low} and SIGLEC-F$^+$[10] (Figures 1B, 1C, and S2, lung panels). Two subsets of AM were identified; 83% ± 5% were RB$^+$, and the remainder expressed only mApple (R$^+$ AMs) (Figure 1C, lung panels). Minor

(B) Representative Uniform Manifold Approximation and Projection (UMAP) plots of spectral cytometry analysis of the monocyte/macrophage compartment show the expression of different surface markers and the three fluorescent reporter expressions and the cluster identification in the five indicated organs. mApple$^+$ECFP$^+$EGFP$^+$ = RGB$^+$ cells (cyan), mApple$^+$ECFP$^-$EGFP$^+$ = RG$^+$cells (green), mApple$^+$ECFP$^-$EGFP$^-$ = R$^+$ (red), mApple$^+$ECFP$^+$EGFP$^-$ = RB$^+$ (blue). cMono, classical monocyte; ncMono, non-classical monocytes; KC, Kupffer cells; AM, alveolar macrophage; RM, renal macrophage; ATM, AT macrophage (visceral); MG, microglia. See also Figures S1–S3.

(C) Pie charts show the relative proportion of the different fluorescent signatures among the dominant tissue-resident macrophages (KC, AM, RM, ATM, and MG), the minor MPs (minor MPs), and the cMono and ncMono. Mean percentages ±SD for each subset are indicated (n = 8 out of two or three independent experiments).

(D) *In vivo* BTP was performed by intravenous (i.v.) injection of anti-CD45 antibody to discriminate monocyte and resident macrophage localization in the blood compartment (ivCD45$^+$) or within the tissue (ivCD45$^-$). ivCD45 positivity threshold was based according to ivCD45 FMO staining control for major MP, minor MP, and total monocytes (gray histograms). Percentage ± SD of intravascular cells (*in vivo* CD45$^+$) is indicated for each subset (n = 7, out of three independent experiments).

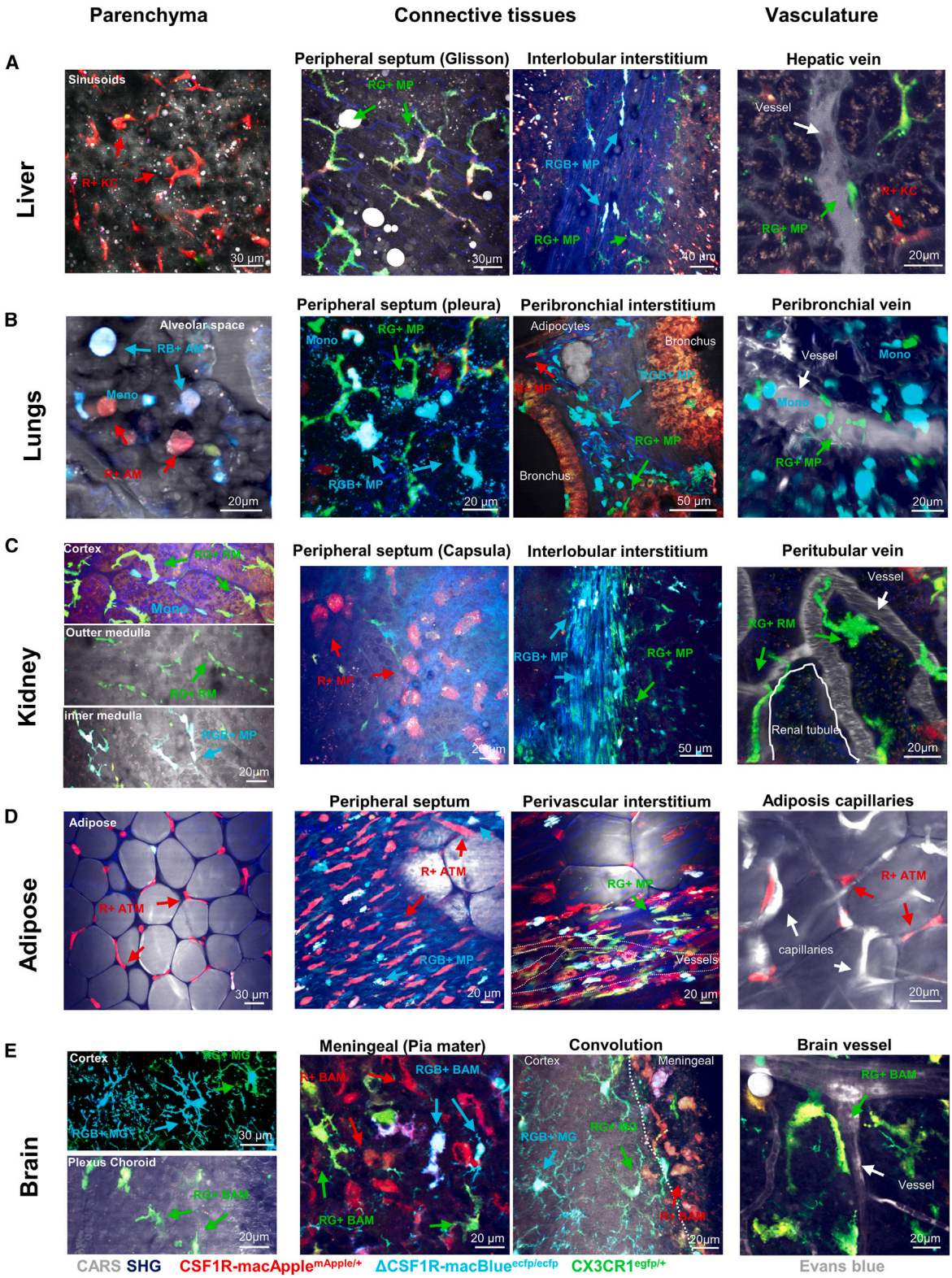

Figure 2. Location of tissue-specific and minor MP populations in the RGB mouse

Representative two-photon laser scanning microscopy (TPLSM) 3D images of (A) liver, (B) lungs, (C) kidney, (D) visceral AT, and (E) brain from fresh explanted tissue show the general distribution of cells according to their fluorescent signatures in the RGB-Mac mouse. To image deeper regions, the organ was cut in the

(legend continued on next page)

macrophage populations in the lung are usually referred as interstitial macrophages.[7,10] Among this population (representing 15% ± 6% of the MP compartment), three subsets, exhibiting the R^+, the RG^+, or the RGB^+ signature, were identified (Figures 1B, 1C, and S2).

In the kidney, the dominant renal resident macrophage subset defined as $CD11b^{low}$ and $F4/80^{high}$, as initially described,[24] were RG^+, consistent with previous analysis using *Cx3cr1*$^{egfp/+}$[31] (Figures 1B, 1C, and S2, kidney panels). Similar to the lung, among the minor MPs (representing 9% ± 2% of the MP compartment), R^+, RG^+, and RGB^+ subsets were detected (Figures 1B, 1C, and S2).

In visceral adipose tissue, 96% of cells in the major macrophage population (AT macrophage [ATM]) (defined as $CD11b^{low}$ $MGL1^+$ $TIM4^+$ $CD206^+$ $CD163^{+/-}$) expressed mApple only (R^+ ATM) (Figures 1B, 1C, and S2). The absence of EGFP is consistent with low expression of *Cx3cr1* mRNA[5] and the limited role of CX3CR1 in ATM accumulation during high-fat-diet-induced obesity.[32] Among the minor MP populations representing 32% ± 8% of the MP compartment, four fluorescent signatures were detected (RGB^+, RG^+, R^+, and RB^+; Figures 1B and 1C), but these populations were not distinguished by any markers other than the reporters (Figures 1B and S2, adipose panels).

Finally, in the brain, as previously reported,[15] two subsets of $CD45^{low}$ $CX3CR1^{high}$ microglia were defined based on ECFP expression (RGB^+ 70%, RG^+ 30%) (Figures 1B, 1C, and S2, brain panels). The minor populations representing border-associated macrophages (BAMs)[33,34] represented 11% ± 6% of the MP compartment and were predominantly RG^+ expressing either MHC-II or CD206 and CD163 and the remainder were R^+ and RGB^+ expressing $CD206^+CD163^+$ but not MHC-II (Figures 1B, 1C, and S2, brain panels).

In each tissue, the relative abundance of monocyte varied among the tissues (Figures 1C and S1B). In each case, ncMonos were over-represented compared to blood circulating monocytes (Figures 1C and S1D). ncMonos are known to exert their patrolling activity by adhering to the abluminal side of the endothelium[35]; hence, ncMonos are likely underrepresented in blood draw compared to tissue samples. Nevertheless, the differential representation of cMono/ncMono across the vascular compartment of the organs might reflect a tissue-dependent vascular accumulation of this subset.

To test this possibility, blood tissue partitioning (BTP) by *in vivo* CD45 intravascular staining[36] was performed (Figure 1D). In tissues other than adipose, cMono and ncMono resided mostly in the vasculature. As expected, KCs residing within liver sinusoids were labeled with anti-CD45, but major macrophage populations in other tissues were not accessible to the injected antibody (Figure 1D). Minor resident MP subsets were expected to be located outside the vasculature. However, anti-CD45 also bound the minor RGB^+ macrophage subset in the liver, the lung, and the kidney, suggesting that they span the vasculature and the parenchyma. A similar subset was defined in the lung as non-classical tissue monocytes.[37]

In overview, heterogeneous expression of the three reporters in the RGB-Mac mouse allows discrimination between monocytes, the major tissue-specific macrophage populations, and minor subsets that can be used to visualize their spatial organization by imaging.

Location of tissue-specific and minor MP populations in the RGB mouse

In order to map the spatial localization and organization of the different identified MPS cells, we conducted multi-photon and spinning-disk imaging of freshly preserved isolated organs, minimizing intervention to preserve 3D tissue structure, cell organization, and morphology and also on thick cryo-sections of fixed organs. Detection of the RGB fluorophores was combined with second harmonic generation (SHG) to detect the collagen of the septa and interstitial connective tissues, coherent anti-Stokes Raman spectroscopy (CARS)[38] to visualize non-fluorescent tissue structures (stroma, adipose, nerves, organized epithelium and endothelium), or natural tissue autofluorescence (elastin fibers, epithelium) with or without complementary vascular labeling using Evans blue. We called this approach "structural imaging" (Figure 2).

In the liver, R^+ cells, mostly corresponding to KCs, were distributed throughout the liver (Figure S4A). These R^+ cells exhibited an elongated morphology, aligning along the lumen of the liver sinusoids as expected for KCs (Figures 2A, S4A, and S4B). Live imaging of the liver confirmed that R^+ KCs remained stationary in the lumen, sampling the flow of red blood cells, while an RGB^+ cell (which could be cMono, ncMono, or a $CLEC4F^-$ MP subset according to flow cytometry) was observed crawling (Video S1). Other elongated RGB^+ and stellar RG^+ MPs were identified at the surface of the liver (the Glisson capsula) and in the interlobular interstitia, which separate the hepatic lobules and contain the vessels and biliary ducts of the hepatic triads (Figures 2A and S4A). These correspond to portal tract macrophages and liver DCs[30] or lipid-associated macrophages and transitioning monocytes.[29]

In the lungs, RB^+ and R^+ AMs were defined by their large, round shape and their localization in alveolar spaces (Figure 2B). High intensity of ECFP expression, the spectrum of which overlaps with the one of EGFP, along with bright autofluorescence, also produce an apparent EGFP signal that was absent in flow cytometry (Figures 2B and S4C). Beyond the difference in shape, size, and locations, AMs could also be discriminated from other RGB^+ and R^+ cells by the CARS signal reflecting a high content of lipid vesicles on two-photon laser-scanning microscopy (TPLSM) images (Figure S4C upper TPLSM images). The two subsets could be detected in close proximity, sometimes sharing the same alveolar sac (Figure 2B). Live imaging of

middle and imaged through the cut side. For all tissues, images show the distribution of the different fluorescent subsets in parenchymal regions (left column) connective-tissue regions (middle columns), and close to vasculature (right column). Connective tissue was visualized through collagen detection by second harmonic generation (SHG). Tissue structures were detected by coherent anti-Stokes Raman spectroscopy (CARS). Evans blue was injected prior to organ collection to visualize vasculature. Dashed line delineates the pia mater from the cortex determined by CARS in brain. Full line delineates the renal tubule from the vasculature. Selected images are representative of more than five mice. Arrows indicate representative cell subsets. See also Figure S4.

alveolar space revealed that, at steady state, AMs were scarcely motile at the surface of the pulmonary epithelium (Video S2). Numerous smaller RGB$^+$ cells with ameboid-shape located between alveoli were most likely the abundant monocytes (Figures 2B and S4C) as detected by cytometry. Live imaging showed their patrolling activity in the lung capillaries, squeezed by the narrow space available and transiently blocking the flow of red blood cells (Video 2). Previous analysis in explanted lungs showed monocytes actively patrolling independently of the blood flow.[39] Some RGB$^+$ MP subsets were also present in collagen-rich structures, detected by SHG of the pleura and around bronchus (Figures 2B and S4C). By contrast, RG$^+$ cells were positioned in stromal regions at the basement of bronchus epithelium and perivascular (Figures 2B and S4C). Finally, we located the rare R$^+$ population in the "broncho-arterial interstitium,"[40] around the artery defined by the typical elastin fiber organization surrounding smooth muscle fibers, detected by SHG and autofluorescence (Figure S4C). TPLSM using CARS further detected adipose accumulations in these regions (Figures 2B and S4C, lower TPLSM image), indicating that lung R$^+$ MPs and RG$^+$ MPs, despite their very close proximity, are associated with different stromal structures.

RG$^+$ cells, representing the major renal macrophage population, were abundantly distributed throughout the kidney (Figure S4D), with an increased concentration from the cortex to the inner medulla confirming previous studies.[41] Renal cortex was identified by the transversal and intermingled organization of renal tubules with high autofluorescence compared to the longitudinal organization of renal tubules and less autofluorescence in the medulla (Figure S4D). Within the medulla, we observed a very distinct separation of RG$^+$ cells and RGB$^+$ cells. The inner zone of the medulla was covered by MP subsets with an RGB$^+$ signature, while the outer area was covered by RG$^+$ cells (Figures 2C and S4D). Outer and inner medulla are functionally distinct regions of the kidney,[42] suggesting a local adaptation of the MPS depending on the anatomic region. Structural imaging of different regions showed that these renal macrophages displayed an elongated morphology in direct contact of renal tubules and tubular capillaries, detected by CARS and autofluorescence (Figures 2C and S4D). This positioning was previously described to allow direct sampling of the bloodstream.[31] Smaller round RGB$^+$ cells located between the renal tubules were assumed to be monocytes within the vasculature (Figure 2C). Live imaging of the kidney confirmed that perivascular RG$^+$ renal macrophages were sessile but exhibited active protrusive activity, while the round RGB$^+$ cells in the vascular compartment were passed rapidly through the imaging field (Video S3). Similar to the liver and the lungs, distinct RGB$^+$ and RG$^+$ cells were also detected in the interstitium, defined by collagen matrix detected by SHG (Figure 2C). Finally, R$^+$ MPs were located in the peripheral septum (capsula) at the surface of the kidney, and around the renal artery embedded in AT (Figures 2C and S4D, TPLSM image).

In the visceral AT, the majority of MPs detected by cytometry expressed only mApple. These R$^+$ cells include the dominant MGL1$^+$CD206$^+$CD163$^{+/-}$ and a minor MGL1$^-$CD206$^-$CD163$^-$ MP subset (Figures 1B and S2, adipose panels). Similar subsets were previously identified depending on their association with blood vessels and their monocytic origin.[43] By imaging, R$^+$ cells were recovered within the parenchyma, flattened between adipocytes and capillaries and in the surrounding connective tissue detected by SHG (Figures 2D and S4E, TPLSM images). CD163 expression was largely restricted to R$^+$ cells in close contact with adipocytes (Figure S4E, lower panels) consistent with previous localization of MGL1$^+$ cells.[25] Beyond that, we could not discriminate the different R$^+$ subsets in the AT, so they were considered as a single population thereafter. Rare RG$^+$ cells and two RB$^+$ and RGB$^+$ subsets were detected in the peripheral connective tissue surrounding the adipose parenchyma (Figures 2D and S4E). Despite the spectral overlap of ECFP in the EGFP channel, RB$^+$ and RGB$^+$ signatures could be discriminated based on the relative intensity in the EGFP channel (Figure S4E, TPLSM images). These two subsets shared similar locations and exhibited a less elongated morphology compared to the R$^+$ cells in the same region (Figures 2D and S4E). Their abundance varied between regions, with some evidence of accumulation forming crown-like structures (Figure S4E, TPLSM images) suggesting they derived from monocytes.[44] In the connective tissue, we noted a progressive loss of ECFP intensity in individual cells suggesting a transition from RB$^+$ to R$^+$ ATMs (Figure S4E, TPLSM images).

In the brain parenchyma, the vast majority of RGB$^+$ and RG$^+$ cells exhibited a typical microglia morphology, characterized by a small cell body and abundant dendritic branching (Figure 2E). No differences in this morphology were detected between RGB$^+$ and RG$^+$ cells. However, a distinct distribution of the two subsets across the tissue was observed in brain cryosections. RGB$^+$ microglia were more abundant in regions related to gray matter (cortex), while RG$^+$ microglia were more represented in regions related to white matter (corpus callosum, cerebellum, periventricular) (Figures S4F and S4G). Structural imaging identified typical BAMs, which differ from microglia in morphology and location (choroid plexus, meningeal and perivascular spaces).[33,34] The rarest RGB$^+$ population was almost exclusively observed in the pia mater, the closest meningeal layer imaged at the very surface of the brain, along with a more abundant R$^+$ subset. These two populations covered the pia mater and were detectable in the cerebral convolutions at the interface between the pia mater and the cortex (Figure 2E), consistent with the identification as meningeal BAM.[33] RG$^+$ cells represented more than half of the BAMs (Figure 1, brain panels). Some RG$^+$ BAMs were found in the choroid plexus and lining brain capillaries (Figures 2E, S4F, and S4H).[33] RG$^+$ BAMs could be divided into CD206$^+$ CD163$^+$MHC-II$^-$ and CD206$^-$MHC-II$^+$ cells (Figure S2). Additional labeling with anti-MHC-II antibody in the brain confirmed that perivascular RG$^+$ cells are the subset expressing MHC-II (Figure S4H).[33]

RGB-Mac mouse discriminates CCR2$^+$, CX3CR1$^+$, and FOLR2$^+$ MPs in distinct tissue territories across organs

Structural imaging of the RGB-Mac mouse revealed that the dominant tissue-specific macrophages, the minor subsets, and the tissue-associated monocytes cover distinct tissue territories in each organ. To extend these findings, we performed a more detailed 3D-imaging of the bilio-vascular[45] interstitium in the liver (regrouping the hepatic triads), the broncho-vascular interstitium

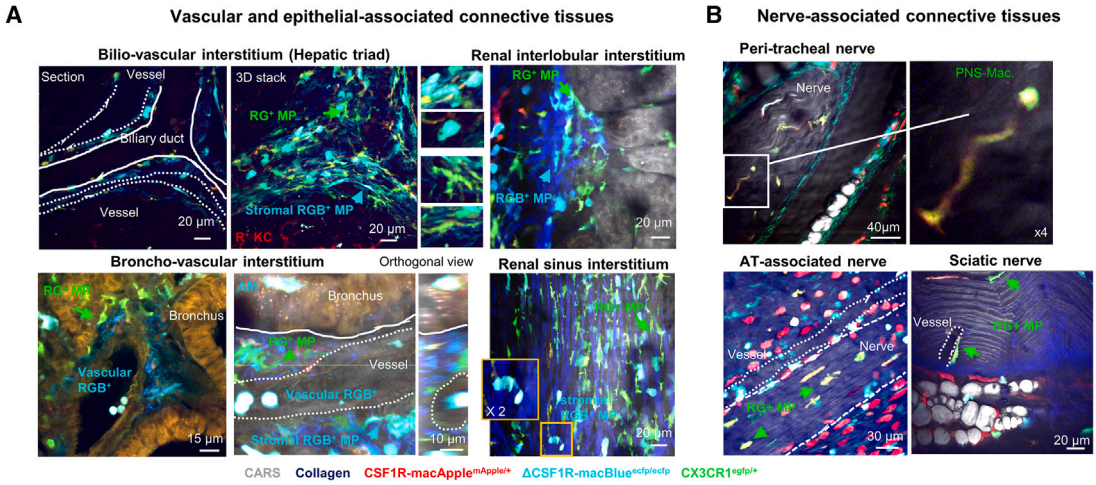

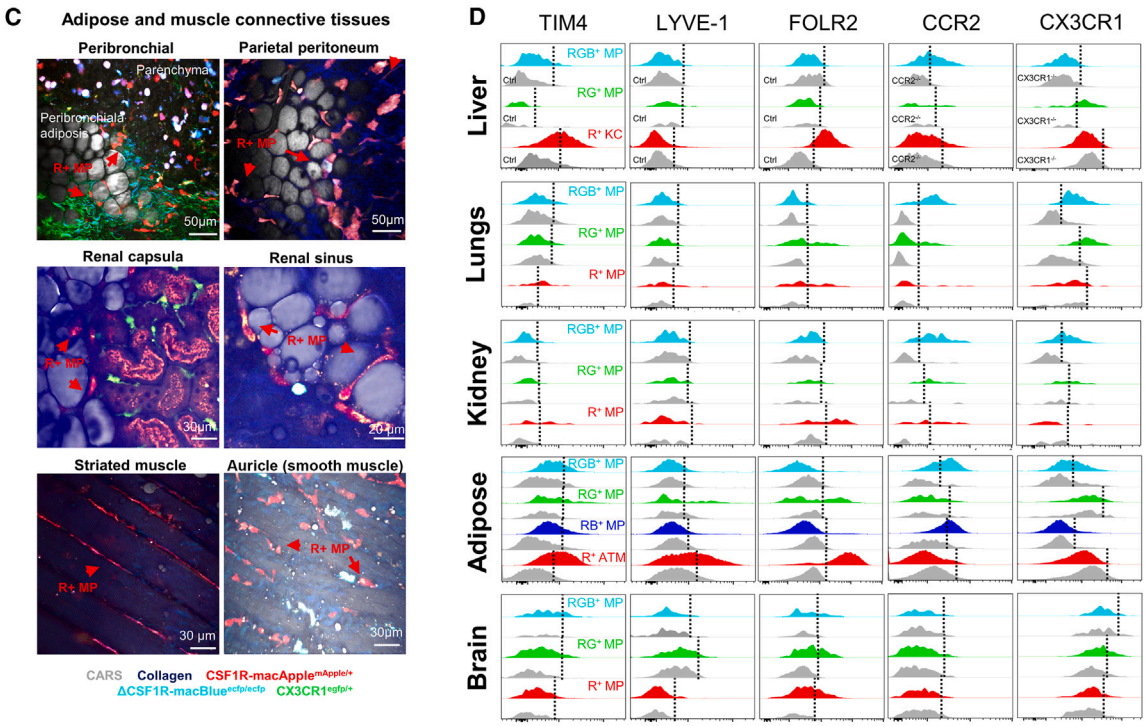

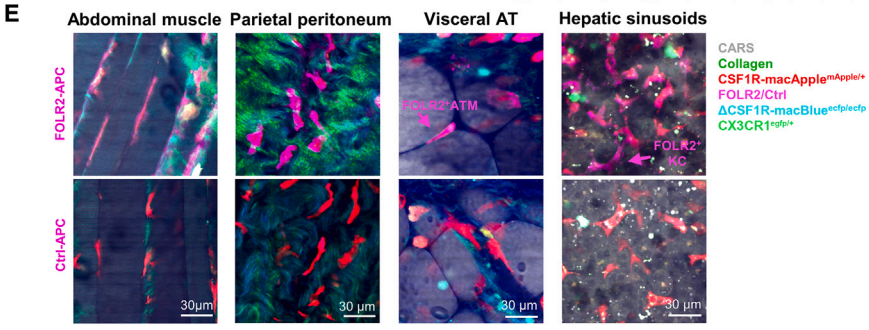

(legend on next page)

in the lungs,[40] and interstitial areas in the kidney (Figure 3A). These interstitia invaginate throughout the tissue to support and guide neuro-vascular branching around bronchial airways for the lungs, biliary ducts in the liver, and collecting ducts in the kidney at the interface with the tissue parenchyma.[46]

In these regions, some RGB$^+$ cells located in the vascular lumen likely correspond to the intravascular monocytes or vascular RGB$^+$ MPs detected by BTP (Figure 1D). Other RGB$^+$ cells exhibited a more elongated morphology, located within the stroma, embedded in collagen matrix (Figures 3A and S5A), confirming BTP analysis (Figure 1D). RG$^+$ cells mostly exhibited a more elongated and stellate shape lying at the basement membrane of the epithelium where small blood vessels could be detected (Figures 3A and S5B). RG$^+$ cells were also observed in the endoneurium of the largest nerves, in very close contact with neurofibers (Figure 3B), akin to what has previously been defined as peripheral nervous system (PNS) macrophages[47] or nerve-associated macrophages (NAMs).[48] Blood vessels and nerves are relatively intermingled as expected (Figure 3B). It is likely that the same cell can be close to both structures. Chakarov et al., demonstrated that similar perivascular and tissue-NAMs represented two independent populations conserved across tissues.[7] By contrast to RG$^+$ cells, R$^+$ cells had a distinct location, in adipose connective tissue within peribronchial regions of the lung but also at the surface of the parietal peritoneum, in the renal capsula and renal sinus (Figure 3C), even in small adipose islets a few micrometers apart of the sciatic nerve (Figure 3B). R$^+$ cells were also found in the perimysium of striated muscle and connective tissue surrounding cardiomyocytes of the cardiac auricle detected by CARS and SHG (Figure 3C).

Overall, the detailed structural imaging of the interstitial MPs confirmed the relatively tight sub-anatomic restriction of the three fluorescent signatures across different tissues, indicating that the diversity of the MP compartment is related to the anatomic organization of the tissue.

We next addressed whether the minor MPS cell subsets could be further discriminated by additional surface markers. We developed a spectral cytometry panel (Figures 1B and S2) aiming to elucidate how the CCR2$^+$, MHC-II$^+$, and TLF$^+$ populations[6] relate to those identified in the RGB-Mac mouse (Figures 3D and S5C).

All subsets expressed CD64, F4/80, and SIRPα (CD172α, an important regulator of phagocytosis[49]) (Figure S5C). Only a fraction expressed CD11c, mostly the RGB$^+$ cells in the liver and kidney (Figure S5C). RGB$^+$ cells exhibited the same fluorescent signature as monocytes and expressed CCR2 in all tissue but the brain (Figure 3D). However, compared to tissue-associated monocytes, RGB$^+$ MPs expressed a similar level of the complement receptor C5AR1/CD88, which was described to discriminate monocytes, macrophages, and DCs in both human and mouse[50,51] but a higher level of MHC-II and various proportions of the ectonucleotidase CD39, emerging as a potent regulator of macrophage polarization[52,53] (Figure S5C). The heterogeneous expression of CD88 and CD39 suggested that the CCR2$^+$ RGB$^+$ MPs represent a variety of subsets that we suspected to be mostly cells undergoing monocyte-derived differentiation.[6]

The TLF core markers (TIM4$^+$ Lyve-1$^+$ FOLR2$^+$), mainly FOLR2 and TIM4, were identified on R$^+$ cells including KCs in the liver and the ATMs, confirming previous transcriptomic analysis indicating the absence of CX3CR1 in these cells.[6] In the adipose tissue, the MGL1$^+$ ATMs co-expressed FOLR2, TIM4, CD163, CD206, and LYVE-1, suggesting a core signature of fat-associated macrophages (Figures 1 and 3D). FOLR2 expression was confirmed by two-photon microscopy on KCs and adipose macrophages after *in situ* injection of specific- or non-specific antibodies on explanted fresh tissues of RGB-Mac mouse. Expression was also detected on R$^+$ cells in the connective tissue of the parietal peritoneum, covering a layer of adipose and the perineurium of muscular fibers (Figure 3E). By default, the RG$^+$ cells could represent the third MHC-II$^+$ subset defined by Dick et al.[6] We confirmed that the expression of EGFP, which is the highest in this subset, mostly correlated with the expression of the CX3CR1 at the membrane serving as a better discriminating marker than MHC-II (Figure 3D). We conclude that subsets expressing CCR2 (RGB$^+$), FOLR2 (R$^+$), or CX3CR1 (RG$^+$), fitting with the three populations defined by Dick et al.,[6] are associated with distinct sub-anatomic structures.

MP populations identified in the RGB mice depend on distinct signaling pathways

To understand homeostatic regulation of MPS subsets in tissues, we examined the effect of loss of function of the major monocyte chemokine receptors, CCR2 and CX3CR1, or antibody-mediated blockade of CSF1R, CSF1, and CSF2. We generated the RGB-Mac mice with homozygous mutations in *Ccr2* or *Cx3cr1* (using the *Cx3cr1*$^{egfp/egfp}$ knockin) or treated RGB-Mac mice with anti-CSF1R, anti-CSF1, anti-CSF2, or

Figure 3. RGB-Mac mouse discriminates CCR2$^+$, CX3CR1$^+$, and FOLR2$^+$ MP in distinct tissue territories across organs

(A) TPLSM 3D images showing the fluorescent signature of resident MP associated with vascular- and epithelial-associated connective tissues in different organs of the RGB-Mac mouse. Dashed and full lines indicate the different tissue structures. Collagen fibers of the stroma are detected by SHG, tissue epithelia are detected by CARS and autofluorescence. Arrows indicate examples of cell subtypes.

(B) TPLSM 3D images showing the fluorescent signature of MP associated with nerves. Arrows indicate the RG$^+$ MP in contact with neurofibers. Collagen fibers of the stroma are detected by SHG. Myelin sheaths of the neurofibers detected by CARS indicate the nerve.[38] Dashed lines indicate the different tissue structures.

(C) TPLSM 3D images showing the fluorescent signature of MP in the stroma associated with adipose and muscular fibers in different organs. Collagen fibers of the stroma are detected by SHG; adipose and muscular fibers are detected by CARS and SHG.

(D) Representative histogram plots by spectral cytometry showing the expression in each organ of the indicated markers for each subset. For the TLF markers (TIM4$^+$, LYVE-1$^+$, FOLR2$^+$), a control antibody (Ctrl) was used to set up the cutoff of positivity staining (dashed lines); for CCR2 and CX3CR1 staining, surface expression was compared for each subset to the one using *Ccr2*$^{-/-}$ and *Cx3cr1*$^{egfp/egfp}$ RGB-Mac mice.

(E) TPLSM 3D images of freshly explanted tissues injected with anti-FOLR2 or Ctrl antibody, showing FOLR2 expression on MP of different regions (upper images) compared to control antibody (bottom images). Collagen fibers of the stroma are detected by SHG; adipose, liver parenchyma, and muscular fibers are detected by CARS. Arrows indicate examples of cell subtypes. TPLSM and spectral cytometry have been reproduced at least three times. See also Figure S5.

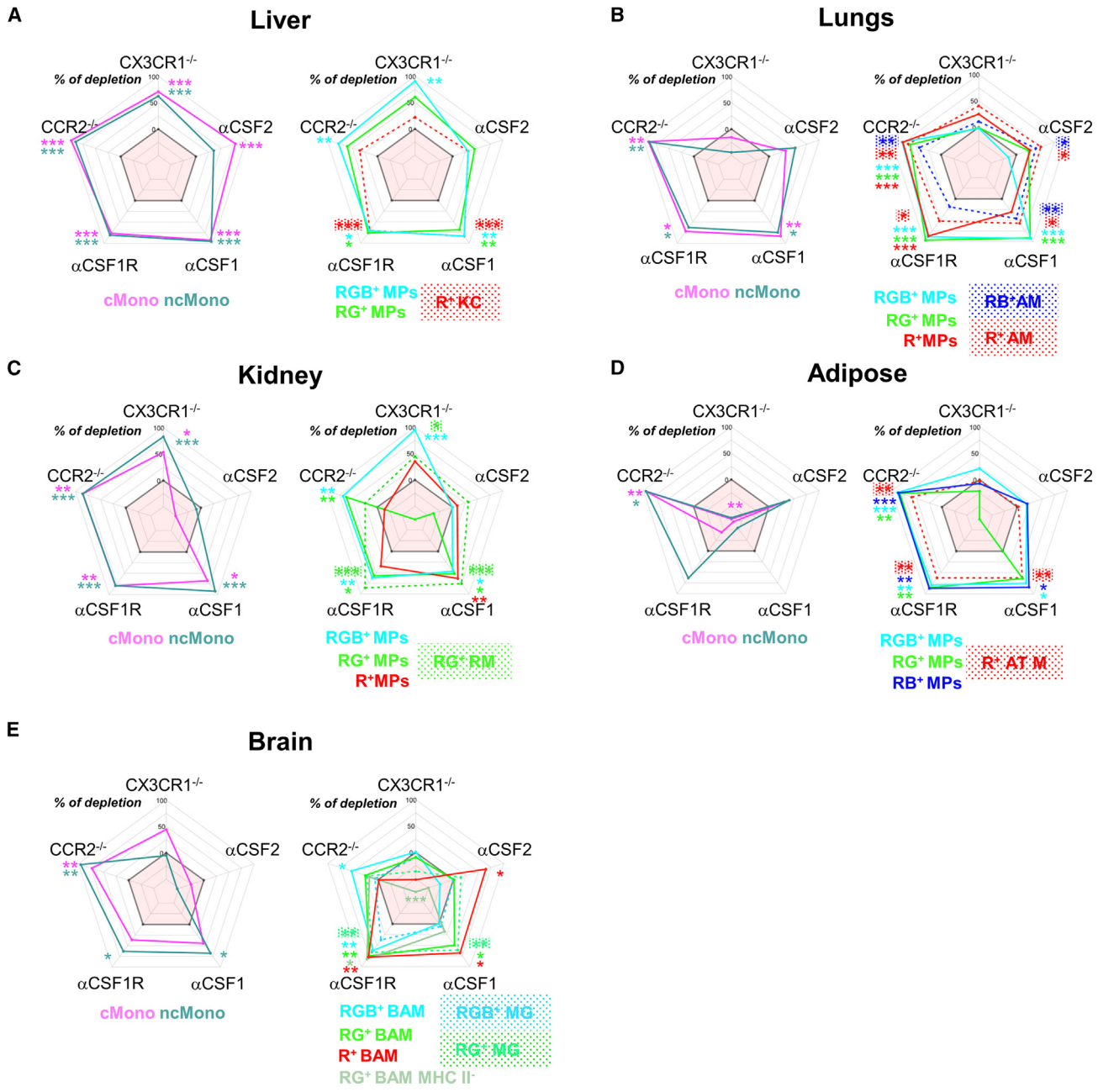

Figure 4. MP populations identified in the RGB-Mac mice depend on distinct signaling pathways

(A–E) Radar charts represent the percentage of depletion of cMono and ncMono (left panels) and macrophages (right panels; tissue-specific resident macrophages [dashed lines], minor MP subsets [full lines]) in *Ccr2*$^{-/-}$ and *Cx3cr1*$^{egfp/egfp}$ RGB-Mac mice and following anti-CSF1R, anti-CSF1, and anti-CSF2 antibody treatments. Pool of wild-type (WT) and isotype control-treated mice was used for reference. Above the reference line, populations were considered depleted compared to control; below the reference line, populations were considered enriched compared to control. Data represent the mean of six to eight mice out of two or three independent experiments. All conditions were compared to the reference for each subset individually. Normality tests were performed to test Gaussian distribution for each subset. When normality tests passed, one-way ANOVA with uncorrected Fisher's least significant difference (LSD) tests were performed. When normality tests did not pass, Kruskal-Wallis with uncorrected Dunn's tests were performed. *$p < 0.05$, **$p < 0.01$, ***$p < 0.001$. No difference was observed between WT and isotype control-treated mice so they were pooled. See also Figures S6–S10.

isotype controls and performed flow cytometry and spinning-disk imaging. The absolute numbers of cells per gram of tissue in each condition were quantified (Figure S6). The percentage of depletion of each subset is shown in (Figure 4).

CX3CR1 and CCR2 are pivotal chemokine receptors that regulate the distribution of monocytes and macrophages. CCR2 controls monocyte release from the bone marrow into the bloodstream, leading to a significant reduction in circulating

monocytes in CCR2-deficient mice.[54] CX3CR1 governs monocyte deployment under steady state and in inflammatory conditions by facilitating margination to the endothelium[55] and regulating the survival of ncMonos.[56] As anticipated, CCR2 deficiency resulted in a decrease in the numbers of tissue-associated cMonos and ncMonos in all organs (Figures 4 and S6). Conversely, monocyte numbers in CX3CR1-deficient mice were reduced only in the liver and kidney, not in the lungs, adipose, and brain, confirming that tissue-associated monocyte accumulation is differentially regulated across organs (Figures 4 and S6).

The RGB$^+$ subsets, expressing CCR2 in every organ but the brain (Figure 3D), were also reduced in CCR2-deficient mice, supporting a monocytic origin. CX3CR1 deficiency reduced the accumulation of this subset only in the liver and the kidney (Figures 4 and S6). The RG$^+$ subset were also affected by CCR2 deficiency in every tissue but to a lesser extent compared to the RGB$^+$ cells (Figures 4 and S6). We further analyzed the effect of CX3CR1 deficiency on the spatial distribution of cells in the kidney. We observed selective loss of RG$^+$ MPs located in the cortex (Figure S7). The reasons for this perturbed distribution can be multiple but support a CX3CR1-dependent regulation of renal macrophage tissue coverage. An important increase in the number of MHC-II$^-$ RG$^+$ MPs was also observed in the brain of *Cx3cr1*$^{egfp/egfp}$ mice and a similar but non-significant tendency regarding RG$^+$ microglia (Figures 4E and S6E), suggesting that CX3CR1 might also be involved in certain regions of the brain. Although CX3CR1 is not essential for the distribution of microglia, it has been shown to participate in the development of thalamocortical synapses.[57] The tissue-specific macrophage populations were also differentially affected by CCR2 and CX3CR1 deficiency. KCs and microglial cells were unaffected. Alveolar and adipose populations were reduced in *Ccr2*$^{-/-}$ but not in *Cx3cr1*$^{egfp/egfp}$, and the pattern was reversed in the kidney (Figures 4 and S6).

Although CSF1R signals are required for the maintenance of tissue macrophages, even prolonged anti-CSF1R treatment does not deplete blood monocytes but blocks development of the non-classical subset.[58] A mouse line lacking expression of CSF1R in monocytes and their progenitors is not monocyte deficient.[59] Anti-CSF1R treatment showed a broad depletion efficacy within 4 days, on both cMonos and ncMonos, in all tissues but the visceral AT (Figures 4 and S6). This suggests that CSF1R signals are required directly or indirectly for monocyte recruitment or persistence in tissues. All tissue-resident macrophages, except RB$^+$ AMs and RGB$^+$ microglia, were also significantly depleted, suggesting that the intraperitoneal antibody treatment reached most regions in these tissues (Figures 4 and S6). The anti-CSF1R-mediated depletion impacted all sub-anatomic regions in the liver (Figure S8A), the AT (Figure S8C), and the kidney (Figures S9A and S9B). In the lung, pleural, and bronchovascular regions, MP depletion was very efficient, while AMs persisted (Figure S8B). In the brain, the remaining macrophages in the cortex were mostly RGB$^+$ microglia. RG$^+$ cells in the choroid plexus and the corpus callosum were also depleted. In the cerebellum, the depletion appeared less severe (Figures S10A and S10B). Whether anti-CSF1R depletion is inferred to CSF1R-signaling blockade or antibody-dependent cellular cytotoxicity is difficult to evaluate, but the differences in the depletion efficacies observed between subsets support the former.

In the liver, R$^+$ KC, RGB$^+$, and RG$^+$ subsets were sensitive to CSF1 but not CSF2 blockade (Figures 4A and S6A), as confirmed by imaging (Figure S8A).

In the lungs, both AM subsets were significantly depleted after CSF1 and CSF2 inhibition, while RGB$^+$, RG$^+$, and R$^+$ interstitial populations were sensitive only to anti-CSF1 (Figures 4B, S6B, and S8B).

In the kidney, all defined subsets were affected by anti-CSF1R and anti-CSF1 and barely affected by anti-CSF2 treatment, in particular the dominant renal macrophage subset, (Figures 4C, S6C, and S9). However, in the inner medulla, numerous RGB$^+$ cells remained after anti-CSF1 treatment, suggesting this subset is neither CSF1 nor CSF2 dependent (Figure S9).

In the visceral AT, the profile was similar to the kidney with all populations depleted by CSF1R and CSF1 blockade and not by CSF2 blockade (Figures 4D, S6D, and S8C). An accumulation of round RGB$^+$ cells could be detected at the surface of the AT predominantly after anti-CSF1 treatment. This accumulation could reflect the accumulation of cMonos and ncMonos detected by flow cytometry (Figure S6D).

In the brain, the dominant RGB$^+$ microglia subset was depleted by CSF1R blockade but not by CSF1 blockade, while the RG$^+$ microglia were significantly depleted by CSF1R and CSF1 blockade (Figures 4E and S6E). This observation aligned with the previous observation showing that microglia of the gray matter depend primarily on interleukin (IL)34, whereas those of the white matter are CSF1 dependent.[60] This preferential reduction of RG$^+$ microglia was striking in the cortex and the corpus callosum but to a lesser extent in the cerebellum (Figure S10B). Regarding BAM, RG$^+$ MHC-II$^+$ and R$^+$ cells were sensitive to anti-CSF1 but RG$^+$ MHC-II$^-$ cells were not (Figures 4E and S6E). Imaging confirmed that pia mater-associated R$^+$ MPs were depleted after anti-CSF1R and anti-CSF1 treatment (Figure S10A), while macrophages in the choroid plexus were depleted by anti-CSF1R but not anti-CSF1 treatment (Figure S10B). The R$^+$ cells were the only BAM population significantly depleted by CSF2 blockade (Figures 4E and S6E). By imaging, anti-CSF2-mediated depletion of this subset was not as evident as after anti-CSF1, as numerous cells persisted with a heterogeneous distribution across different fields (Figure S10A).

These observations highlight that the homing and maintenance of tissue-associated monocytes and the diverse resident MPs are differentially dependent on CSF1, CSF2, CX3CR1, and CCR2 across organs and even within the same tissue. This underscores the adaptation of each subset to its local environment at the sub-anatomic level.

Recovery of monocyte, tissue-specific, and interstitial macrophage populations after chemical ablation

We next explored the relative ability of macrophage subsets to recover following treatment with cyclophosphamide (CP), a well-defined alkylating agent that leads to myelo-ablation in the bone marrow followed by a rebound monocytosis.[61] We quantified subpopulations defined by the transgenic reporters at different time points in each organ following a single dose of

CP and monitored their spatial distribution during their recovery phase (Figures 5 and S11). Tissue-associated cMonos and ncMonos declined to a nadir 3 days after CP and recovered, with an overshoot for cMonos, by day 7. After 21 days, their numbers returned to normal steady state in the liver, lungs, and kidney but remained elevated in the AT and the brain (Figure S11). Accumulation of small round RGB$^+$ cells (monocyte-like) was detected at the periphery of all tissue in hepatic triads and sinusoids (Figure S12A), in the alveolar space of the lungs (Figure S12B), in the cortex and outer medulla of the kidney (Figure S13), and in the AT (Figure S12C). In the brain, the accumulation of monocyte-like RGB$^+$ cells was only detected in the vasculature of the pia mater (Figure S12D). Tissue-specific and connective-tissue-associated MPs from all organs including the brain were sensitive to CP, with maximum depletion reached at day 7 for the liver, lungs, and kidney (Figures 5A–5C), while adipose and brain macrophages had already started to recover at this time (Figures 5D and 5E).

R$^+$ KCs and RGB$^+$ MPs recovered fast, but less so than RG$^+$ MPs (Figure 5A). These last accumulated in the hepatic triads (Figure S12A). CP treatment led to a reduction in the global density of KCs over the liver parenchyma at day 7, and their recovery between day 7 and day 21 was homogeneous with no notable difference compared to control at day 21 (Figure S12A).

In the lungs, RB$^+$ AMs showed faster reconstitution than their R$^+$ counterparts (Figure 5B). AMs, defined as the large round cells located on airways, were detected in alveolar space but relatively absent in large bronchus airways at day 7 and 14 and were found again at day 21 (Figure S12B). RG$^+$ cells of the pleura were already reconstituted at day 14, while R$^+$ and RG$^+$ cells surrounding the broncho-vascular regions recovered as in control by day 21 (Figure S12B).

Kidney MPs were the slowest to recover, and their counts were still significantly depleted at day 21 (Figure 5C). RG$^+$ cells in the cortex and RGB$^+$ cells in the inner medulla were selectively depleted compared to RG$^+$ cells in the outer medulla (Figure S13). Between days 7 and 14, some RGB$^+$ cells with elongated morphology progressively accumulated in the cortex, a likely intermediate in replacement of the RG$^+$ cells (Figure S13). RG$^+$ cells in the cortex were finally back at day 21 (Figure S13) in accordance with flow cytometry quantification (Figure 5C).

RB$^+$ and RGB$^+$ cells in the adipose appeared prior to R$^+$ ATMs (Figure 5D). Within 14 days, R$^+$ ATMs were fully restored in both the periphery and within the AT parenchyma (Figure S12C). RB$^+$ and RGB$^+$ cells exhibiting protrusions (distinct from round monocyte-like RGB$^+$ cells) were detected in clusters, mostly at the surface of the AT (Figure S12C). The different levels of ECFP expression in these clusters further supports the idea of a differentiation series whereby RGB$^+$ monocytes first lose EGFP expression then ECFP.

In the brain, the depletion of RGB$^+$ and RG$^+$ microglia was striking (Figure 5E). The remaining cells exhibited a perturbed morphology with less dendritic extensions at day 7 compared to control (Figure S12D). Between day 14 and 21, microglia recovered their morphology and their abundance (Figures 5E and S12D). In contrast, meningeal R$^+$ cells located at the surface were barely affected by CP treatment (Figures 5E and S12D).

In conclusion, following chemo-mediated ablation, each MPS cell subset recovered its abundance and spatial distribution following chemical ablation, demonstrating a high homeostatic regulation of the territorial coverage across all sub-anatomic compartments.

DISCUSSION

Macrophages within tissues occupy a niche or territory. Their regular distribution within tissues may be partly cell autonomous and partly defined by interactions with other cells or extracellular matrix.[3,12,62] In this study, we developed a structural imaging approach that enabled the direct visualization of MPs at single-cell resolution within their physiological environment, preserving the sub-anatomic structure of blood vessels, nerves, adiposes, epithelium, and capsular or interstitial stroma. Non-tissue-specific macrophages are commonly designated under the generic term of interstitial macrophages, although the term interstitium is poorly defined. We showed a relatively distinct compartmentalization of the interstitial MPs from tissue-specific macrophages and uncovered a previously undefined level of sub-anatomic diversity in tissue interstitia, including adipose islets, epithelial layers (e.g., bronchus tracts, biliary duct), nerves, and smooth or striated muscle fibers, sometimes all very intricate but each apparently harboring a dedicated MP population. This level of information is more challenging to obtain in multiplexed immunofluorescence or mass imaging technologies that rely on thin tissue sections. In the RGB-Mac mouse, the fluorescent signatures aligned with the three conserved macrophage populations (CCR2$^+$, MHC-II$^+$, and TLF$^+$), defined by Dick et al.[6] The RGB$^+$ MPs locating either in the vasculature or within the interstitium demonstrated distinct phenotypic features compared to cMonos and ncMonos but expressed the same fluorescent signature as well as CCR2. Their abundance was reduced in *Ccr2*-knockout (KO) mice, suggesting a monocyte origin. The TLF$^+$ population[6] overlaps the R$^+$ signature of the RGB-Mac mouse. In most tissue, R$^+$ subsets expressed FOLR2 and TIM4. Structural imaging enabled the detection of AT surrounding organs such as the kidney, the surface of the peritoneum, and in the proximity of peri-bronchial arteria. The presence of these adipose islets has been described to alleviate mechanical constraints but might also serve as a source of energy in accordance with a major role of macrophages in metabolic regulation.[63] Finally, R$^+$ MPs were also found in perimysium covering muscular fibers and on cardiac macrophages along cardiomyocytes of the auricle, consistent with the detection of FOLR2 on cardiac macrophages.[6] Whether FOLR2$^+$ macrophages from distinct tissues (KCs, ATMs, and muscular-associated MPs) share similar functional roles deserves further investigation but they define a group of macrophages that do not express CX3CR1. The R$^+$ signature in the RGB-Mac mouse allows the direct visualization of the FOLR2$^+$ macrophage compartment across tissues, which cannot be observed through the *Cx3cr1*$^{egfp/+}$ mouse reporter, confirming that FOLR2$^+$ and CX3CR1$^+$ macrophages represent two distinct compartments and conferring to the RGB-Mac mouse a complete picture in the mapping of resident MP.

The factors regulating the expression of the fluorescent reporters are not yet clear. There is evidence suggesting that

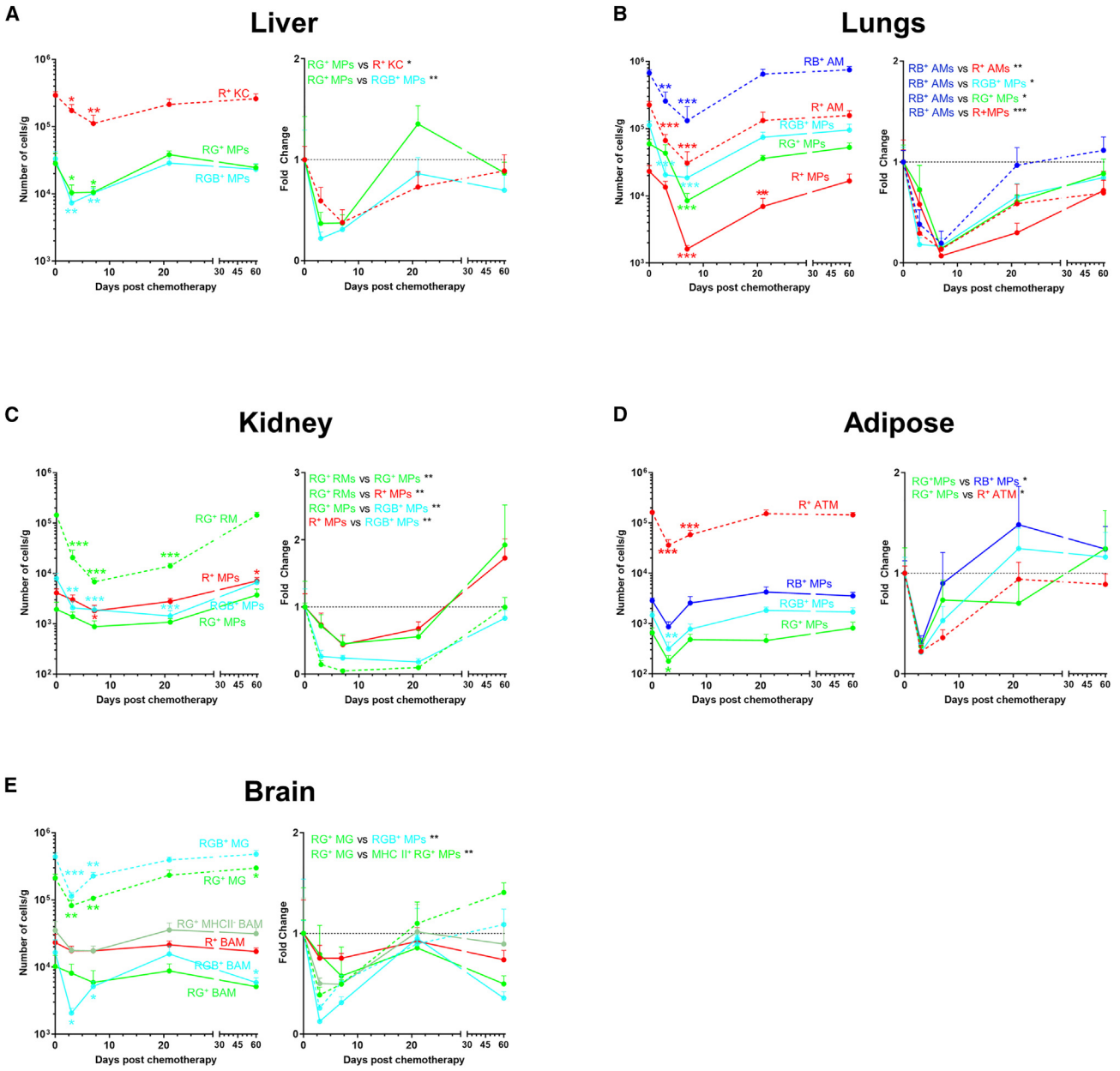

Figure 5. Recovery of monocyte, tissue-specific macrophage, and interstitial macrophage populations after chemical ablation

The effect of chemotherapy (175 mg/kg) was monitored over time on dominant tissue-resident macrophage subsets (dashed line) and the minor MP (full lines) in (A) the liver, (B) the lungs, (C) the kidney, (D) the visceral AT, and (E) the brain. In each tissue, absolute numbers of cells per milligram of tissue were quantified by flow cytometry (left panels) and fold change compared to untreated mice was represented (right panels). Graphs represent mean ± SEM of $n = 6$ mice out of two independent experiments; one-way ANOVA with Fischer LSD tests were performed to compare absolute numbers after treatment to the absolute number of untreated control mice. Areas under the curve were calculated to compare differences in the recovery ability of the different TRM subsets in each organ (right panels). $^{*}p < 0.05$, $^{**}p < 0.01$, $^{***}p < 0.001$. See also Figures S11–S13.

RGB$^+$ MPs can lose ECFP expression upon differentiation, notably in the intestinal lamina propria where there is continuous monocyte infiltration.[20] It is likely that a similar progressive loss of ECFP and EGFP gives rise to the monocyte-derived RG$^+$ and R$^+$ populations in certain conditions. The expression of ECFP in the MacBlue transgene is suspected to reflect the activation of the AP1 transcription factor induced by CSF1 to sustain *Csf1r* transcription.[20,64] Some tissue macrophages retain ECFP expression, suggesting distinct regulation of *Csf1r* transcription. This is consistent with the notion that the local environment shapes tissue-resident macrophage enhancer landscapes.[65]

Microglia and AMs are the only ECFP^{+} tissue-specific macrophages known to rely mainly on IL-34 and CSF2, respectively. Interestingly, we found that both populations exhibited ECFP^{-} counterparts with slightly different sensitivity to anti-CSF1 or anti-CSF1R. In each case, there is evidence of heterogeneity that may not be due to different stages of differentiation. The observation that RG^{+} microglia are enriched in white matter and selectively depleted by anti-CSF1 treatment is consistent with evidence of a distinct transcriptomic signature in white-matter microglia.[66] In the kidney, ECFP expression was restricted to the inner medulla and RGB^{+} subset was relatively insensitive to anti-CSF1 but depleted by anti-CSF1R. This suggests a possible role for IL-34 expression in the kidney.[67] The identification of the molecular factors differentially involved in the regulation of tissue-specific and the various interstitial MPs will offer an opportunity to target them more specifically depending on the pathophysiological context.

We conclude that the composition of the monocyte and macrophage compartment in non-lymphoid organs is dictated by the diversity of tissue structures, including the ratio between the connective-tissue structure and parenchyma, as well as the abundance of blood vessels, nerves, adipose, and muscular fibers. At steady state, each subset appears restricted to specific tissue territories with distinct molecular dependencies. Identifying macrophages according to these distinct territories will help to better understand their functional diversity in pathological contexts, particularly their functional adaptation upon tumor development.

Limitations of the study

Although the fluorescent reporters of the RGB-Mac mouse have been widely used in different settings, it is important to note that they do not tag only MPs. Despite lower expression of the fluorescent reporters, these other subsets (neutrophils mApple/ECFP^{low}, NK/T cells EGFP^{+}) can be contaminating depending on the context. The combination of the three fluorescent reporters contributes to a more accurate identification of the different subsets along with cell size, morphology, and fluorescence intensity. The reasons why macrophage subsets differentially expressed the fluorescent reporters as a result of their localization is still unclear but reflects tissue-specific homeostatic signals.

RESOURCE AVAILABILITY

Lead contact

Further information and requests for resources and reagents should be directed to Alexandre Boissonnas (alexandre.boissonnas@upmc.fr).

Materials availability

The RGB-Mac line and the parent MacApple line generated in this study are available from the lead contact without restriction. We are glad to share these mouse lines with reasonable compensation by requestor for processing and shipping.

Data and code availability

- Data reported in this paper are available from the lead contact upon reasonable request.
- This paper does not report original code.
- Any additional information required to reanalyze the data reported in this paper is available from the lead contact upon request.

ACKNOWLEDGMENTS

We would like to thank the reviewers for their important contribution to improving the quality of this manuscript. This work was supported by Association pour la Recherche contre le Cancer ARC "Projet labellisé", Fondation BMS 2022, ANR-21-CE14-0067-01, ANR-23-CE14-0019, and Program "Emergence-Sorbonne Université"; INCa (2018-1-PLBIO-06-1) supported M.P. with funding. D.A.H. is supported by NHMRC (Australia) Investigator Grant 2009750. The authors thank UMS28 for the animal core facility and the two-photon microscopy and Christelle Enond and Thomas Van Hecke for animal breeding.

The authors are grateful to Dormeur Foundation, Vaduz, for providing the Cryostat HM550 apparatus.

AUTHOR CONTRIBUTIONS

Investigation and formal analysis, M.P., E.W.-D., F.L., and A.B.; investigation, S.B., M.F., O.B., and N.G.; provision of resources, D.A.H., C.C., and A.B.; writing – review & editing, M.P., E.W.-D., O.B., DA.H., C.C., and A.B.; conceptualization and supervision, C.C. and A.B.; project administration and funding acquisition, A.B.

DECLARATION OF INTERESTS

The authors declare no competing interests.

STAR★METHODS

Detailed methods are provided in the online version of this paper and include the following:

- KEY RESOURCES TABLE
- EXPERIMENTAL MODEL AND STUDY PARTICIPANT DETAILS
  - Mice
  - Ethical statement
- METHOD DETAILS
  - Antibody treatment and chemotherapy
  - Blood/tissue partitioning and sample preparation
  - Spectral and conventional flow cytometry
  - Structural and live multi-photon imaging
  - Confocal imaging
- QUANTIFICATION AND STATISTICAL ANALYSIS

SUPPLEMENTAL INFORMATION

Supplemental information can be found online at https://doi.org/10.1016/j.celrep.2024.114847.

Received: March 25, 2024
Revised: August 3, 2024
Accepted: September 23, 2024
Published: October 10, 2024

REFERENCES

1. Lazarov, T., Juarez-Carreño, S., Cox, N., and Geissmann, F. (2023). Physiology and diseases of tissue-resident macrophages. Nature *618*, 698–707. https://doi.org/10.1038/s41586-023-06002-x.
2. Okabe, Y., and Medzhitov, R. (2016). Tissue biology perspective on macrophages. Nat. Immunol. *17*, 9–17. https://doi.org/10.1038/ni.3320.
3. Hume, D.A., Irvine, K.M., and Pridans, C. (2019). The Mononuclear Phagocyte System: The Relationship between Monocytes and Macrophages. Trends Immunol. *40*, 98–112. https://doi.org/10.1016/j.it.2018.11.007.

4. Mass, E., Nimmerjahn, F., Kierdorf, K., and Schlitzer, A. (2023). Tissue-specific macrophages: how they develop and choreograph tissue biology. Nat. Rev. Immunol. *23*, 563–579. https://doi.org/10.1038/s41577-023-00848-y.

5. Summers, K.M., Bush, S.J., and Hume, D.A. (2020). Network analysis of transcriptomic diversity amongst resident tissue macrophages and dendritic cells in the mouse mononuclear phagocyte system. PLoS Biol. *18*, e3000859. https://doi.org/10.1371/journal.pbio.3000859.

6. Dick, S.A., Wong, A., Hamidzada, H., Nejat, S., Nechanitzky, R., Vohra, S., Mueller, B., Zaman, R., Kantores, C., Aronoff, L., et al. (2022). Three tissue resident macrophage subsets coexist across organs with conserved origins and life cycles. Sci. Immunol. *7*, eabf7777. https://doi.org/10.1126/sciimmunol.abf7777.

7. Chakarov, S., Lim, H.Y., Tan, L., Lim, S.Y., See, P., Lum, J., Zhang, X.M., Foo, S., Nakamizo, S., Duan, K., et al. (2019). Two distinct interstitial macrophage populations coexist across tissues in specific subtissular niches. Science *363*, eaau0964. https://doi.org/10.1126/science.aau0964.

8. Dutertre, C.-A., Becht, E., Irac, S.E., Khalilnezhad, A., Narang, V., Khalilnezhad, S., Ng, P.Y., van den Hoogen, L.L., Leong, J.Y., Lee, B., et al. (2019). Single-Cell Analysis of Human Mononuclear Phagocytes Reveals Subset-Defining Markers and Identifies Circulating Inflammatory Dendritic Cells. Immunity *51*, 573–589.e8. https://doi.org/10.1016/j.immuni.2019.08.008.

9. Hume, D.A., Millard, S.M., and Pettit, A.R. (2023). Macrophage heterogeneity in the single-cell era: facts and artifacts. Blood *142*, 1339–1347. https://doi.org/10.1182/blood.2023020597.

10. Gibbings, S.L., Thomas, S.M., Atif, S.M., McCubbrey, A.L., Desch, A.N., Danhorn, T., Leach, S.M., Bratton, D.L., Henson, P.M., Janssen, W.J., and Jakubzick, C.V. (2017). Three Unique Interstitial Macrophages in the Murine Lung at Steady State. Am. J. Respir. Cell Mol. Biol. *57*, 66–76. https://doi.org/10.1165/rcmb.2016-0361OC.

11. Li, X., Mara, A.B., Musial, S.C., Kolling, F.W., Gibbings, S.L., Gerebtsov, N., and Jakubzick, C.V. (2024). Coordinated chemokine expression defines macrophage subsets across tissues. Nat. Immunol. *25*, 1110–1122. https://doi.org/10.1038/s41590-024-01826-9.

12. Guilliams, M., Thierry, G.R., Bonnardel, J., and Bajenoff, M. (2020). Establishment and Maintenance of the Macrophage Niche. Immunity *52*, 434–451. https://doi.org/10.1016/j.immuni.2020.02.015.

13. Laviron, M., Combadière, C., and Boissonnas, A. (2019). Tracking Monocytes and Macrophages in Tumors With Live Imaging. Front. Immunol. *10*, 1201. https://doi.org/10.3389/fimmu.2019.01201.

14. Laviron, M., Petit, M., Weber-Delacroix, E., Combes, A.J., Arkal, A.R., Barthélémy, S., Courau, T., Hume, D.A., Combadière, C., Krummel, M.F., and Boissonnas, A. (2022). Tumor-associated macrophage heterogeneity is driven by tissue territories in breast cancer. Cell Rep. *39*, 110865. https://doi.org/10.1016/j.celrep.2022.110865.

15. Hawley, C.A., Rojo, R., Raper, A., Sauter, K.A., Lisowski, Z.M., Grabert, K., Bain, C.C., Davis, G.M., Louwe, P.A., Ostrowski, M.C., et al. (2018). *Csf1r*-mApple Transgene Expression and Ligand Binding In Vivo Reveal Dynamics of CSF1R Expression within the Mononuclear Phagocyte System. J. Immunol. *200*, 2209–2223. https://doi.org/10.4049/jimmunol.1701488.

16. Sasmono, R.T., Oceandy, D., Pollard, J.W., Tong, W., Pavli, P., Wainwright, B.J., Ostrowski, M.C., Himes, S.R., and Hume, D.A. (2003). A macrophage colony-stimulating factor receptor-green fluorescent protein transgene is expressed throughout the mononuclear phagocyte system of the mouse. Blood *101*, 1155–1163, [pii]. https://doi.org/10.1182/blood-2002-02-0569.

17. Jung, S., Aliberti, J., Graemmel, P., Sunshine, M.J., Kreutzberg, G.W., Sher, A., and Littman, D.R. (2000). Analysis of fractalkine receptor CX(3)CR1 function by targeted deletion and green fluorescent protein reporter gene insertion. Mol. Cell Biol. *20*, 4106–4114.

18. Ovchinnikov, D.A., van Zuylen, W.J.M., DeBats, C.E.E., Alexander, K.A., Kellie, S., and Hume, D.A. (2008). Expression of Gal4-dependent transgenes in cells of the mononuclear phagocyte system labeled with enhanced cyan fluorescent protein using Csf1r-Gal4VP16/UAS-ECFP double-transgenic mice. J. Leukoc. Biol. *83*, 430–433, [pii]. https://doi.org/10.1189/jlb.0807585.

19. Ovchinnikov, D.A., DeBats, C.E.E., Sester, D.P., Sweet, M.J., and Hume, D.A. (2010). A conserved distal segment of the mouse CSF-1 receptor promoter is required for maximal expression of a reporter gene in macrophages and osteoclasts of transgenic mice. J. Leukoc. Biol. *87*, 815–822. https://doi.org/10.1189/jlb.0809557.

20. Sauter, K.A., Pridans, C., Sehgal, A., Bain, C.C., Scott, C., Moffat, L., Rojo, R., Stutchfield, B.M., Davies, C.L., Donaldson, D.S., et al. (2014). The MacBlue binary transgene (csf1r-gal4VP16/UAS-ECFP) provides a novel marker for visualisation of subsets of monocytes, macrophages and dendritic cells and responsiveness to CSF1 administration. PLoS One *9*, e105429, [pii]. https://doi.org/10.1371/journal.pone.0105429.

21. Grabert, K., Sehgal, A., Irvine, K.M., Wollscheid-Lengeling, E., Ozdemir, D.D., Stables, J., Luke, G.A., Ryan, M.D., Adamson, A., Humphreys, N.E., et al. (2020). A Transgenic Line That Reports CSF1R Protein Expression Provides a Definitive Marker for the Mouse Mononuclear Phagocyte System. J. Immunol. *205*, 3154–3166. https://doi.org/10.4049/jimmunol.2000835.

22. Sasmono, R.T., Ehrnsperger, A., Cronau, S.L., Ravasi, T., Kandane, R., Hickey, M.J., Cook, A.D., Himes, S.R., Hamilton, J.A., and Hume, D.A. (2007). Mouse neutrophilic granulocytes express mRNA encoding the macrophage colony-stimulating factor receptor (CSF-1R) as well as many other macrophage-specific transcripts and can transdifferentiate into macrophages in vitro in response to CSF-1. J. Leukoc. Biol. *82*, 111–123. https://doi.org/10.1189/jlb.1206713.

23. Wolf, A.A., Yáñez, A., Barman, P.K., and Goodridge, H.S. (2019). The Ontogeny of Monocyte Subsets. Front. Immunol. *10*, 1642. https://doi.org/10.3389/fimmu.2019.01642.

24. Hume, D.A., Robinson, A.P., MacPherson, G.G., and Gordon, S. (1983). The mononuclear phagocyte system of the mouse defined by immunohistochemical localization of antigen F4/80. Relationship between macrophages, Langerhans cells, reticular cells, and dendritic cells in lymphoid and hematopoietic organs. J. Exp. Med. *158*, 1522–1536.

25. Lumeng, C.N., DelProposto, J.B., Westcott, D.J., and Saltiel, A.R. (2008). Phenotypic switching of adipose tissue macrophages with obesity is generated by spatiotemporal differences in macrophage subtypes. Diabetes *57*, 3239–3246. https://doi.org/10.2337/db08-0872.

26. Harrison, J.K., Jiang, Y., Chen, S., Xia, Y., Maciejewski, D., McNamara, R.K., Streit, W.J., Salafranca, M.N., Adhikari, S., Thompson, D.A., et al. (1998). Role for neuronally derived fractalkine in mediating interactions between neurons and CX3CR1-expressing microglia. Proc. Natl. Acad. Sci. USA *95*, 10896–10901.

27. Ginhoux, F., Liu, K., Helft, J., Bogunovic, M., Greter, M., Hashimoto, D., Price, J., Yin, N., Bromberg, J., Lira, S.A., et al. (2009). The origin and development of nonlymphoid tissue CD103+ DCs. J. Exp. Med. *206*, 3115–3130, [pii]. https://doi.org/10.1084/jem.20091756.

28. Liu, Z., Gu, Y., Chakarov, S., Bleriot, C., Kwok, I., Chen, X., Shin, A., Huang, W., Dress, R.J., Dutertre, C.-A., et al. (2019). Fate Mapping via Ms4a3-Expression History Traces Monocyte-Derived Cells. Cell *178*, 1509–1525.e19. https://doi.org/10.1016/j.cell.2019.08.009.

29. Guilliams, M., Bonnardel, J., Haest, B., Vanderborght, B., Wagner, C., Remmerie, A., Bujko, A., Martens, L., Thoné, T., Browaeys, R., et al. (2022). Spatial proteogenomics reveals distinct and evolutionarily conserved hepatic macrophage niches. Cell *185*, 379–396.e38. https://doi.org/10.1016/j.cell.2021.12.018.

30. English, K., Tan, S.Y., Kwan, R., Holz, L.E., Sierro, F., McGuffog, C., Kaisho, T., Heath, W.R., MacDonald, K.P., McCaughan, G.W., et al. (2022). The liver contains distinct interconnected networks of CX3CR1^{+} macrophages, XCR1^{+} type 1 and CD301a^{+} type 2 conventional dendritic cells embedded within portal tracts. Immunol. Cell Biol. *100*, 394–408. https://doi.org/10.1111/imcb.12559.

31. Stamatiades, E.G., Tremblay, M.-E., Bohm, M., Crozet, L., Bisht, K., Kao, D., Coelho, C., Fan, X., Yewdell, W.T., Davidson, A., et al. (2016). Immune Monitoring Of Trans-Endothelial Transport By Kidney Resident Macrophages. Cell *166*, 991–1003. https://doi.org/10.1016/j.cell.2016.06.058.

32. Morris, D.L., Oatmen, K.E., Wang, T., DelProposto, J.L., and Lumeng, C.N. (2012). CX3CR1 Deficiency Does Not Influence Trafficking of Adipose Tissue Macrophages in Mice With Diet-Induced Obesity. Obesity *20*, 1189–1199. https://doi.org/10.1038/oby.2012.7.

33. Van Hove, H., Martens, L., Scheyltjens, I., De Vlaminck, K., Pombo Antunes, A.R., De Prijck, S., Vandamme, N., De Schepper, S., Van Isterdael, G., Scott, C.L., et al. (2019). A single-cell atlas of mouse brain macrophages reveals unique transcriptional identities shaped by ontogeny and tissue environment. Nat. Neurosci. *22*, 1021–1035. https://doi.org/10.1038/s41593-019-0393-4.

34. Silvin, A., Qian, J., and Ginhoux, F. (2023). Brain macrophage development, diversity and dysregulation in health and disease. Cell. Mol. Immunol. *20*, 1277–1289. https://doi.org/10.1038/s41423-023-01053-6.

35. Auffray, C., Fogg, D., Garfa, M., Elain, G., Join-Lambert, O., Kayal, S., Sarnacki, S., Cumano, A., Lauvau, G., and Geissmann, F. (2007). Monitoring of blood vessels and tissues by a population of monocytes with patrolling behavior. Science *317*, 666–670.

36. Anderson, K.G., Mayer-Barber, K., Sung, H., Beura, L., James, B.R., Taylor, J.J., Qunaj, L., Griffith, T.S., Vezys, V., Barber, D.L., and Masopust, D. (2014). Intravascular staining for discrimination of vascular and tissue leukocytes. Nat. Protoc. *9*, 209–222. https://doi.org/10.1038/nprot.2014.005.

37. Schyns, J., Bai, Q., Ruscitti, C., Radermecker, C., De Schepper, S., Chakarov, S., Farnir, F., Pirottin, D., Ginhoux, F., Boeckxstaens, G., et al. (2019). Non-classical tissue monocytes and two functionally distinct populations of interstitial macrophages populate the mouse lung. Nat. Commun. *10*, 3964. https://doi.org/10.1038/s41467-019-11843-0.

38. Boissonnas, A., Louboutin, F., Laviron, M., Loyher, P.L., Reboussin, E., Barthelemy, S., Réaux-Le Goazigo, A., Lobsiger, C.S., Combadière, B., Mélik Parsadaniantz, S., and Combadière, C. (2020). Imaging resident and recruited macrophage contribution to Wallerian degeneration. J. Exp. Med. *217*, e20200471. https://doi.org/10.1084/jem.20200471.

39. Rodero, M.P., Poupel, L., Loyher, P.L., Hamon, P., Licata, F., Pessel, C., Hume, D.A., Combadière, C., and Boissonnas, A. (2015). Immune surveillance of the lung by migrating tissue monocytes. Elife *4*, e07847. https://doi.org/10.7554/eLife.07847.

40. Weber, E., Sozio, F., Borghini, A., Sestini, P., and Renzoni, E. (2018). Pulmonary lymphatic vessel morphology: a review. Ann. Anat. *218*, 110–117. https://doi.org/10.1016/j.aanat.2018.02.011.

41. Hume, D.A., and Gordon, S. (1983). Mononuclear phagocyte system of the mouse defined by immunohistochemical localization of antigen F4/80. Identification of resident macrophages in renal medullary and cortical interstitium and the juxtaglomerular complex. J. Exp. Med. *157*, 1704–1709.

42. Wei, G., Rosen, S., Dantzler, W.H., and Pannabecker, T.L. (2015). Architecture of the human renal inner medulla and functional implications. Am. J. Physiol. Renal Physiol. *309*, F627–F637. https://doi.org/10.1152/ajprenal.00236.2015.

43. Silva, H.M., Báfica, A., Rodrigues-Luiz, G.F., Chi, J., Santos, P.D.A., Reis, B.S., Hoytema van Konijnenburg, D.P., Crane, A., Arifa, R.D.N., Martin, P., et al. (2019). Vasculature-associated fat macrophages readily adapt to inflammatory and metabolic challenges. J. Exp. Med. *216*, 786–806. https://doi.org/10.1084/jem.20181049.

44. Cox, N., and Geissmann, F. (2020). Macrophage ontogeny in the control of adipose tissue biology. Curr. Opin. Immunol. *62*, 1–8. https://doi.org/10.1016/j.coi.2019.08.002.

45. Lei, L., Bruneau, A., El Mourabit, H., Guégan, J., Folseraas, T., Lemoinne, S., Karlsen, T.H., Hoareau, B., Morichon, R., Gonzalez-Sanchez, E., et al. (2022). Portal fibroblasts with mesenchymal stem cell features form a reservoir of proliferative myofibroblasts in liver fibrosis. Hepatology *76*, 1360–1375. https://doi.org/10.1002/hep.32456.

46. Benias, P.C., Wells, R.G., Sackey-Aboagye, B., Klavan, H., Reidy, J., Buonocore, D., Miranda, M., Kornacki, S., Wayne, M., Carr-Locke, D.L., and Theise, N.D. (2018). Structure and Distribution of an Unrecognized Interstitium in Human Tissues. Sci. Rep. *8*, 4947. https://doi.org/10.1038/s41598-018-23062-6.

47. Wang, P.L., Yim, A.K.Y., Kim, K.-W., Avey, D., Czepielewski, R.S., Colonna, M., Milbrandt, J., and Randolph, G.J. (2020). Peripheral nerve resident macrophages share tissue-specific programming and features of activated microglia. Nat. Commun. *11*, 2552. https://doi.org/10.1038/s41467-020-16355-w.

48. Ural, B.B., Yeung, S.T., Damani-Yokota, P., Devlin, J.C., De Vries, M., Vera-Licona, P., Samji, T., Sawai, C.M., Jang, G., Perez, O.A., et al. (2020). Identification of a nerve-associated, lung-resident interstitial macrophage subset with distinct localization and immunoregulatory properties. Sci. Immunol. *5*, eaax8756. https://doi.org/10.1126/sciimmunol.aax8756.

49. Feng, Y., Huang, C., Wang, Y., and Chen, J. (2023). SIRPα: A key player in innate immunity. Eur. J. Immunol. *53*, 2350375. https://doi.org/10.1002/eji.202350375.

50. Leach, S.M., Gibbings, S.L., Tewari, A.D., Atif, S.M., Vestal, B., Danhorn, T., Janssen, W.J., Wager, T.D., and Jakubzick, C.V. (2020). Human and Mouse Transcriptome Profiling Identifies Cross-Species Homology in Pulmonary and Lymph Node Mononuclear Phagocytes. Cell Rep. *33*, 108337. https://doi.org/10.1016/j.celrep.2020.108337.

51. Mulder, K., Patel, A.A., Kong, W.T., Piot, C., Halitzki, E., Dunsmore, G., Khalilnezhad, S., Irac, S.E., Dubuisson, A., Chevrier, M., et al. (2021). Cross-tissue single-cell landscape of human monocytes and macrophages in health and disease. Immunity *54*, 1883–1900.e5. https://doi.org/10.1016/j.immuni.2021.07.007.

52. Cohen, H.B., Briggs, K.T., Marino, J.P., Ravid, K., Robson, S.C., and Mosser, D.M. (2013). TLR stimulation initiates a CD39-based autoregulatory mechanism that limits macrophage inflammatory responses. Blood *122*, 1935–1945. https://doi.org/10.1182/blood-2013-04-496216.

53. Rothweiler, S., Feldbrügge, L., Jiang, Z.G., Csizmadia, E., Longhi, M.S., Vaid, K., Enjyoji, K., Popov, Y.V., and Robson, S.C. (2019). Selective deletion of ENTPD1/CD39 in macrophages exacerbates biliary fibrosis in a mouse model of sclerosing cholangitis. Purinergic Signal. *15*, 375–385. https://doi.org/10.1007/s11302-019-09664-3.

54. Serbina, N.V., and Pamer, E.G. (2006). Monocyte emigration from bone marrow during bacterial infection requires signals mediated by chemokine receptor CCR2. Nat. Immunol. *7*, 311–317, [pii]. https://doi.org/10.1038/ni1309.

55. Hamon, P., Loyher, P.L., Baudesson de Chanville, C., Licata, F., Combadière, C., and Boissonnas, A. (2017). CX3CR1-dependent endothelial margination modulates Ly6C^{high} monocyte systemic deployment upon inflammation in mice. Blood *129*, 1296–1307. https://doi.org/10.1182/blood-2016-08-732164.

56. Landsman, L., Bar-On, L., Zernecke, A., Kim, K.W., Krauthgamer, R., Shagdarsuren, E., Lira, S.A., Weissman, I.L., Weber, C., and Jung, S. (2009). CX3CR1 is required for monocyte homeostasis and atherogenesis by promoting cell survival. Blood *113*, 963–972. https://doi.org/10.1182/blood-2008-07-170787.

57. Hoshiko, M., Arnoux, I., Avignone, E., Yamamoto, N., and Audinat, E. (2012). Deficiency of the Microglial Receptor CX3CR1 Impairs Postnatal Functional Development of Thalamocortical Synapses in the Barrel Cortex. J. Neurosci. *32*, 15106–15111. https://doi.org/10.1523/JNEUROSCI.1167-12.2012.

58. MacDonald, K.P.A., Palmer, J.S., Cronau, S., Seppanen, E., Olver, S., Raffelt, N.C., Kuns, R., Pettit, A.R., Clouston, A., Wainwright, B., et al. (2010). An antibody against the colony-stimulating factor 1 receptor depletes the resident subset of monocytes and tissue- and tumor-associated macrophages but does not inhibit inflammation. Blood *116*, 3955–3963. https://doi.org/10.1182/blood-2010-02-266296.

59. Rojo, R., Raper, A., Ozdemir, D.D., Lefevre, L., Grabert, K., Wollscheid-Lengeling, E., Bradford, B., Caruso, M., Gazova, I., Sánchez, A., et al. (2019). Deletion of a Csf1r enhancer selectively impacts CSF1R expression and development of tissue macrophage populations. Nat. Commun. *10*, 3215. https://doi.org/10.1038/s41467-019-11053-8.

60. Easley-Neal, C., Foreman, O., Sharma, N., Zarrin, A.A., and Weimer, R.M. (2019). CSF1R Ligands IL-34 and CSF1 Are Differentially Required for Microglia Development and Maintenance in White and Gray Matter Brain Regions. Front. Immunol. *10*, 2199.

61. Jacquelin, S., Licata, F., Dorgham, K., Hermand, P., Poupel, L., Guyon, E., Deterre, P., Hume, D.A., Combadière, C., and Boissonnas, A. (2013). CX3CR1 reduces Ly6Chigh-monocyte motility within, and release from the bone marrow after chemotherapy in mice. Blood *122*, 674–683. https://doi.org/10.1182/blood-2013-01-480749.

62. Jenkins, S.J., and Hume, D.A. (2014). Homeostasis in the mononuclear phagocyte system. Trends Immunol. *35*, 358–367. https://doi.org/10.1016/j.it.2014.06.006.

63. Dalmas, E., Clément, K., and Guerre-Millo, M. (2011). Defining macrophage phenotype and function in adipose tissue. Trends Immunol. *32*, 307–314. https://doi.org/10.1016/j.it.2011.04.008.

64. Himes, S.R., Sester, D.P., Ravasi, T., Cronau, S.L., Sasmono, T., and Hume, D.A. (2006). The JNK Are Important for Development and Survival of Macrophages. J. Immunol. *176*, 2219–2228. https://doi.org/10.4049/jimmunol.176.4.2219.

65. Lavin, Y., Winter, D., Blecher-Gonen, R., David, E., Keren-Shaul, H., Merad, M., Jung, S., and Amit, I. (2014). Tissue-Resident Macrophage Enhancer Landscapes Are Shaped by the Local Microenvironment. Cell *159*, 1312–1326. https://doi.org/10.1016/j.cell.2014.11.018.

66. Safaiyan, S., Besson-Girard, S., Kaya, T., Cantuti-Castelvetri, L., Liu, L., Ji, H., Schifferer, M., Gouna, G., Usifo, F., Kannaiyan, N., et al. (2021). White matter aging drives microglial diversity. Neuron *109*, 1100–1117.e10. https://doi.org/10.1016/j.neuron.2021.01.027.

67. Baek, J.-H., Zeng, R., Weinmann-Menke, J., Valerius, M.T., Wada, Y., Ajay, A.K., Colonna, M., and Kelley, V.R. (2015). IL-34 mediates acute kidney injury and worsens subsequent chronic kidney disease. J. Clin. Invest. *125*, 3198–3214. https://doi.org/10.1172/JCI81166.

68. Mizuguchi, T., and Nuriya, M. (2020). Applications of second harmonic generation (SHG)/sum-frequency generation (SFG) imaging for biophysical characterization of the plasma membrane. Biophys. Rev. *12*, 1321–1329. https://doi.org/10.1007/s12551-020-00768-4.

69. De Silva, N.S., Siewiera, J., Alkhoury, C., Nader, G.P.F., Nadalin, F., de Azevedo, K., Couty, M., Izquierdo, H.M., Bhargava, A., Conrad, C., et al. (2023). Nuclear envelope disruption triggers hallmarks of aging in lung alveolar macrophages. Nat. Aging *3*, 1251–1268. https://doi.org/10.1038/s43587-023-00488-w.

STAR★METHODS

KEY RESOURCES TABLE

REAGENT or RESOURCE	SOURCE	IDENTIFIER
Antibodies		
InVivoMab anti-mouse CSF1R	BioXcell	Cat#BE0213; RRID:AB_2687699
InVivoMab rat IgG2a isotype control, anti-trinitrophenol	Bioxcell	Cat#BE0089; RRID:AB_1107769
InVivoMab anti-mouse CSF1	BioXcell	Cat#BE0204; RRID:AB_10950309
InVivoMab anti-mouse GM-CSF	BioXcell	Cat#BE0259; RRID: AB_2687738
InVivoMab rat IgG1 isotype control, anti-horseradish peroxidase	BioXcell	Cat#BE088; RRID:AB_1107775
PerCP-Cy5.5 Anti-mouse CD45 (Clone: 30-F11)	BD Biosciences	Cat# 550995; RRID:AB_394003
PE Anti-mouse MHCII (Clone: AF6-120.1)	BD Biosciences	Cat# 553552; RRID:AB_394919
BUV395 Anti-mouse CD11b (Clone: M1/70)	BD Biosciences	Cat#563553; RRID: AB_2738276
Brillant Violet 750 Anti-mouse CCR2 (Clone: 475301)	BD Biosciences	Cat#747967; RRID: AB_2872428
APC Anti-mouse FOLR2 (Clone: 10/FR2)	Biolegend	Cat#153306; RRID:AB_2721313
BUV563 Anti-mouse Ly-6G (Clone: 1A8)	BD Biosciences	Cat#612921; RRID:AB_2870206
PE Anti-mouse CD88 (Clone: 20/70)	Biolegend	Cat#135806; RRID:AB_2243735
Alexa Fluor 647 Anti-mouse CD31 (Clone: 390)	Biolegend	Cat#102416; RRID:AB_493410
APC/Fire 810 Anti-mouse CD45 (Clone: 30-F11)	Biolegend	Cat#103174; RRID:AB_2860600
Alexa Fluor 647 Anti-mouse CLEC4F (Clone: 3E3F9)	Biolegend	Cat#156804; RRID:AB_2814082
eFluor 450 Anti-mouse LYVE1 (Clone: ALY7)	eBioscience	Cat#48-0443-82; RRID: AB_2784723
Brillant Violet 650 Anti-mouse CD206 (Clone: C068C2)	Biolegend	Cat#141723; RRID:AB_2562445
Alexa Fluor 647 Anti-mouse CD39 (Clone: Duha59)	Biolegend	Cat#143808; RRID:AB_2563978
PerCP Anti-mouse Ly-6C (Clone: HK1.4)	Biolegend	Cat#128028; RRID:AB_10897805
Pe/Cyanine7 Anti-mouse MGL1 (Clone: LOM-8.7)	Biolegend	Cat#145609; RRID:AB_2566028
BUV661 Anti-mouse CD103 (Clone: M290)	BD Biosciences	Cat#741504; RRID:AB_2870960
Brillant Violet 510 Anti-mouse I-A/I-E (Clone: M5/114.15.2)	Biolegend	Cat#107635; RRID:AB_2561397
Brillant Violet 570 Anti-mouse CD11c (Clone: N418)	Biolegend	Cat#117331; RRID:AB_10900261
BB700 Anti-mouse Sirpa (Clone: P84)	BD Biosciences	Cat#742205; RRID:AB_2871427

(*Continued on next page*)

Continued

REAGENT or RESOURCE	SOURCE	IDENTIFIER
Brillant Violet 605 Anti-mouse TIM4 (Clone: RMT4-54)	BD Biosciences	Cat#745206; RRID:AB_2742799
APC Anti-mouse CD163 (Clone: S15049I)	Biolegend	Cat#155305; RRID:AB_2814059
Brillant Violet 421 Anti-mouse CD163 (Clone: S15049I)	Biolegend	Cat#155309; RRID:AB_2814063
PE-CF594 Anti-mouse Siglec-F (Clone: E50-2440)	BD Biosciences	Cat#562757; RRID:AB_2687994
BUV737 Anti-mouse CD43 (Clone: S7)	BD Biosciences	Cat#612840; RRID:AB_2870162
Brillant Violet 711 Anti-mouse CX3CR1 (Clone: SA011F11)	Biolegend	Cat#149031; RRID:AB_2565939
APC-R700 Anti-mouse F4/80 (Clone: T45-2342)	BD Biosciences	Cat#565787; RRID:AB_2869711
Brillant Violet 786 Anti-mouse CD64 (Clone: X54-5/7.1)	BD Biosciences	Cat#741024; RRID:AB_2740644
ViaDye Red Fixable Viability Dye Kit	Cytek	Cat#SKU R7-60008
Biotin Anti-mouse NK-1.1 (Clone: PK136)	BD Biosciences	Cat#553163; RRID:AB_394675
Biotin Anti-mouse CD3e (Clone: 500A2)	BD Biosciences	Cat#553239; RRID:AB_394728
Biotin Anti-mouse CD19 (Clone: 1D3)	BD Biosciences	Cat#553784; RRID:AB_395048
Biotin Anti-mouse CD5 (Clone: 53–7.3)	BD Biosciences	Cat#553019; RRID:AB_394557
Biotin Anti-mouse CD4 (Clone: GK1.5)	BD Biosciences	Cat#553728; RRID:AB_395012
Biotin Anti-mouse CD45R/B220 (Clone: RA3-6B2)	BD Biosciences	Cat#553086; RRID:AB_394615
Biotin Anti-mouse CD8a (Clone: 53–6.7)	BD Biosciences	Cat#553029; RRID:AB_394566
PE-Cy5 Streptavidin	BD Biosciences	Cat#554062; RRID:AB_10053563
Chemicals, peptides, and recombinant proteins		
Dnase I	Roche	Cat#10104159001
Dispase II	Gibco	Cat#17105041
Collegenase IV	Gibco	Cat#17104019
Tissue freezing medium (OCT)	Microm-Microtech	Cat#F/TFM-C
Polybeads carboxylate microsphere	Polysciences	Cat#07759-15
Sucrose	Biosolve	Cat#192223
Vectashield with DAPI	VectorLabs	Cat#H-1200-10
Cyclophosphamide monohydrate	Sigma-Aldrich	Cat#C0768
True-Stain Monocyte Blocker	Biolegend	Cat#426103
Evans Blue	Sigma Aldrich	Cat#314-13-6
Mouse BD Fc Block	BD Biosciences	Cat#553141; RRID:AB_394656
Formaldehyde	Sigma	Cat#47608
Experimental models: Organisms/strains		
Mouse: Cx3cr1$^{EGFP/Kin}$	The Jackson laboratory	RRID:IMSR_JAX:005582
Mouse: Csf1rmApple	https://doi.org/10.4049/jimmunol.1701488	Developed by D. Hume
Mouse: ΔCsf1rECFP	https://doi.org/10.1189/jlb.0807585	Developed by D. Hume
Mouse: *Ccr2*$^{-/-}$	The Jackson laboratory	RRID:IMSR_JAX:004999

(*Continued on next page*)

Continued

REAGENT or RESOURCE	SOURCE	IDENTIFIER
Software and algorithms		
Prism v7	GraphPad Software	https://www.graphpad.com/scientific-software/prism/; RRID:SCR_002798
FlowJo v10	FlowJo, Treestar Inc.	https://www.flowjo.com/solutions/flowjo; RRID:SCR_008520
SpectroFlo v3.1.0	Cytek Biosciences	https://cytekbio.com/pages/spectro-flo
OMIQ	OMIQ inc.	https://www.omiq.ai/
Zeiss Zen	Carl Zeiss	http://www.zeiss.com
Diva	BD Biosciences	https://www.bdbiosciences.com/en-us/products/software/instrument-software/bd-facsdiva-software
Imaris v8.0.2	-	http://www.bitplane.com/imaris/imaris RRID:SCR_007370

EXPERIMENTAL MODEL AND STUDY PARTICIPANT DETAILS

Mice

Cx3cr1$^{egfp/+}$,[17] Csf1r-Gal4VP16/UAS-ECFP,[18] Csf1r-mApple[15] were intercrossed to generate the RGB-mac mouse strains. *Ccr2* knock-out (KO) and *Cx3cr1* KO RGB-Mac mouse were generated respectively, by intercrossing RGB-Mac mice with *Ccr2*$^{-/-}$ mice and using homozygous expression of *Cx3cr1*$^{egfp/egfp}$ knock-in. All mice were bred at the Center d'Exploration Fonctionnelle Pitié-Salpêtrière animal facility. All mice were maintained under SPF conditions at 22°C. Males and females between 5 and 7 months old were used. No difference in the abundance of tissue-specific macrophages, other mononuclear phagocytes and monocytes were noticed, so the sexes were pooled.

Ethical statement

All experiment protocols were approved by the French animal experimentation and ethics committee and validated by Service Protection et Santé Animales, Environnement with the number #16890. Sample sizes were chosen to assure reproducibility of the experiments and according to the 3 Rs of animal ethic regulation.

METHOD DETAILS

Antibody treatment and chemotherapy

400μg of anti-CSF1R antibody (AFS98, BioXcell) or rat IgG2a κ isotype control (Clone 2A3, Bioxcell) were administered intraperitoneally three days before harvesting the organs. Anti-CSF1 (5A1, BioXcell), anti-CSF2 (MP1-22E9, BioXcell) or isotype control (IgG1-clone HPRN, IgG2a κ-clone 2A3, BioXcell) were administered intraperitoneally with single shots of 500, 300 and 300 μg at respectively four days, two days and 12 h before collecting the organs. Data from isotype control injected mice were pooled. Cyclophosphamide (CP, Sigma-Aldrich) was injected at 175 mg/kg in the peritoneal cavity.

Blood/tissue partitioning and sample preparation

For flow cytometry, intravascular CD45 labeling was performed according to.[36] Mice were injected intravenously with 1 μg of anti-CD45 PercP-Cy5.5 antibody (clone 30-F11, BD Bioscience). Two minutes after injection, blood was drawn and mice were sacrificed rapidly. Liver, lungs, kidney, visceral adipose tissue and brain were harvested and bathed in a large volume of PBS. Enzymatic digestions of all organs were processed the same way. All tissues were chopped and enzymatically digested with 0.1 mg/mL DNase I (Sigma-Aldrich), 1.5 U/ml Dispase II (Gibco), and 200 U/ml Collagenase Type IV (Gibco) in PBS 1X (Gibco) for 30 min at 37°C under agitation. Samples were filtered using 70mm cell strainer and washed with PBS 1X.

Spectral and conventional flow cytometry

Cell suspensions were first incubated with true monocyte blocker (Biolegend) and Fc blocking agent (BD) for 10 min and then a panel of indicated antibodies (referenced in the key resource table) at room temperature for an additional 20 min. Cells were then washed once in PBS 1X and analyzed directly by flow cytometry. For phenotypic analysis, data were acquired by spectral cytometry (Aurora, Cytek) and analyzed with OMIQ software (Omiq inc.) for UMAP representation (https://omiq.ai, Santa clara CA) or FlowJo software (Tree Star Inc., Ashland, OR, USA). For quantification of cell numbers data were acquired using a restricted antibody panel on the flow cytometer FACS LSRFortessa X-20 (BD Biosciences, Franklin Lakes, NJ, USA) with DIVA (BD Biosciences). Calculation of absolute cell number was performed by adding to each vial a fixed number (10.000) of non-fluorescent 10 μm polybead carboxylate

microspheres (Polysciences, Niles, IL, USA) according to the formula: Number of cells = (Number of acquired cells x 10000)/(Number of acquired beads). Number of cells obtained for each sample was normalized per gram of tissue.

Structural and live multi-photon imaging

The two-photon laser-scanning microscopy (TPLSM) set-up used was a 7MP (Carl Zeiss) coupled to a Ti: Sapphire Crystal, a 140-femtosecond rate, pulsed near-infrared light laser (ChameleonU, Coherent), selectively tunable between 680 and 1050 nm and an optical parametric oscillator (OPO-MPX, Coherent) selectively tunable between 1050 and 1600 nm. The NLO and the OPO beams were spatially aligned and temporally synchronized using a delay line (Coherent) allowing CARS imaging approach. The excitation wavelength was 820 nm for the NLO beam and 1070 nm for the OPO beam to detect the vibrational signature of lipid rich structures at a frequency of 2850 cm^{-1} with an emission wavelength at 665 nm. Temporal synchronization of the beams provided a third excitation ray by the combination of one photon of each beam according to the principle of sum-frequency generation (SFG) (equivalent to 928 nm)[68] allowing a better discrimination of ECFP and EGFP. The system included a set of external non-descanned detectors in reflection with a combination of an LP-600-nm followed by LP-462-nm and LP-500-nm dichroic mirrors to split the light and collect the second harmonic generation signal (SHG) and ECFP with a 480-/40-nm emission filter, EGFP with a 525-/50-nm emission filter, mApple or PE conjugated antibodies with a 624-/40-nm emission filter and CARS, Evans blue or Alexa 647/APC conjugated antibodies signals with an LP 645nm emission filter. To separate CARS and Alexa 647/APC signals, a first image was recorded using the synchronized beams at 820 and 1070 to detect CARS and a second image was recorded using only the OPO beam at 1200 nm to detect only the Alexa 647/APC signal.

Structural 3D imaging was performed on freshly explanted tissue from RGB-Mac mice. For deeper region imaging organs were cut in the middle and imaged toward the sectioned area. For all images the objective was a water immersion, plan apochromat 320 (numerical aperture = 1). For z stack images, slices were acquired every 1 to 3 μm depth depending on the tissue structure acquired and 3D reconstructions were done using Imaris software (Bitplane). The delimitations of tissue structures were indicated by dashed lines in the images based on CARS, SHG and autofluorescence of the 2D or 3D images. Additional antibody staining was performed by injecting directly into the fresh explanted organ, 50μL of PBS 1X with 2μg of anti-CD31-Alexa647, anti-FOLR2-APC, anti-CD163-APC, anti-MHC II-PE antibodies or control antibodies of the same color (to discriminate non-specific binding and autofluorescence) and left for 20 min at RT. The organ was then bathed in PBS for 10 min and directly imaged after.

Live lung imaging was performed as previously described.[69] For liver and kidney live imaging, ventilation was not required. Mice were anesthetized and maintained during the imaging period with 2% isoflurane in medical air, liver and kidney were imaged using the same imaging window than for the lung after small abdominal incisions above the organs. Real time movies were performed by imaging every 3s during 10–15 min.

Confocal imaging

In brief, organs were harvested and fixed in 2% PFA for 6 h and then incubated in 30% sucrose-PBS 1X overnight at 4°C before being embedded in OCT-freezing medium (Microm Microtech, France) and frozen at −80C. Sectioning was completed on an HM550 Cryostat (Microm Microtech, France) at −20°C; 5-μm or 100-μm sections were collected on Superfrost Plus Slides (Thermo Fisher Scientific) and stored at −20°C until use. Slides were counterstained and mounted with Vectashield Mounting Medium with DAPI (Vector Laboratories). Confocal images were acquired on a spinning disk microscope Nikon Eclipse TI2E microscope (Nikon Corporation, Japon) linked with a Crest X-Light V3 (CrestOptic, Italie) using Nikon NIS-elements software. ECFP, EGFP, DAPI and mApple signals were acquired using a combination of laser by CELESTA Light Engine (Lumencor, USA) and emission filters: laser 405nm, EmBP 405/10 for DAPI; laser 440, EmBP460/25 for ECFP; laser 488, EmBP 510/20 for EGFP; laser 546, EmBP 603/30 for mApple. Images were analyzed using Imaris software (Bitplane).

QUANTIFICATION AND STATISTICAL ANALYSIS

All statistical analyses were performed with Graphpad Prism 7. For absolute cell number quantifications and percentages of depletion, normality tests (D'Agostino-Pearson and Shapiro-Wilk) were performed to test Gaussian distribution for each subset. When normality tests passed, one-way ANOVA with uncorrected Fisher's LSD tests were performed. When normality tests did not pass, Kruskal-Wallis with uncorrected Dunn's tests were performed. For chemotherapy recovery the Area under curves (AUC) of the normalized data and the number of cells compared to untreated mice were compared by one-way ANOVA with uncorrected Fisher's LSD test. For all figures *, $p < 0.05$; **, $p < 0.01$; ***, $p < 0.001$. Sample sizes are indicated in each figure legend.